HATSOPOULOS MICROFLUIDS LABORATORY
Department of Mechanical Engineering, Massachusetts Institute of Technology

The Inertio-Elastic Planar Entry Flow of Low-Viscosity Elastic Fluids in Micro-fabricated Geometries

Lucy E. Rodd, Timothy P. Scott, David V. Boger,
Justin J. Cooper-White, Gareth H. McKinley

December 17, 2004
HML Report Number 04-P-03

HML@MIT
http://web.mit.edu/fluids

The Inertio-Elastic Planar Entry Flow of Low-Viscosity Elastic Fluids in Micro-fabricated Geometries

Lucy E. Rodd[1,3], Timothy P. Scott[3], David V. Boger[1],
Justin J. Cooper-White[2], Gareth H. McKinley[3]

[1]Dept. of Chemical and Biomolecular Engineering,
The University of Melbourne, VIC 3010, Australia

[2]Division of Chemical Engineering,
The University of Queensland, Brisbane, QLD 4072, Australia

[3]Hatsopoulos Microfluids Laboratory, Dept. of Mechanical Engineering,
Massachusetts Institute of Technology, Cambridge, MA 02139, USA

December 17, 2004

The non-Newtonian flow of dilute aqueous polyethylene oxide (PEO) solutions through microfabricated planar abrupt contraction-expansions is investigated. The contraction geometries are fabricated from a high-resolution chrome mask and cross-linked PDMS gels using the tools of soft-lithography. The small length scales and high deformation rates in the contraction throat lead to significant extensional flow effects even with dilute polymer solutions having time constants on the order of milliseconds. The dimensionless extra pressure drop across the contraction increases by more than 200% and is accompanied by significant upstream vortex growth. Streak photography and video-microscopy using epifluorescent particles shows that the flow ultimately becomes unstable and three-dimensional. The moderate Reynolds numbers ($0.03 \leq Re \leq 44$) associated with these high Deborah number ($0 \leq De \leq 600$) microfluidic flows results in the exploration of new regions of the *Re-De* parameter space in which the effects of both elasticity and inertia can be observed. Understanding such interactions will be increasingly important in microfluidic applications involving complex fluids and can best be interpreted in terms of the elasticity number, $El = De/Re$, which is independent of the flow kinematics and depends only on the fluid rheology and the characteristic size of the device.

1.0 INTRODUCTION

The high deformation rates and high elasticity numbers achievable in micro-fabricated devices can result in strong viscoelastic effects even in dilute aqueous polymer solutions. This is particularly relevant to lab-on-a-chip [1] and inkjet printing heads, which typically utilize non-Newtonian fluids. The study of micron-scale fluid phenomena in microfluidic devices has been prompted by developments in lab-on-a-chip technology, for which the primary intention has been to facilitate the miniaturisation of several bio-analytical processes onto a single integrated device, which would ultimately separate, transport and sequence DNA samples. Common features of microfluidic experiments are very low Reynolds numbers, low Peclet numbers, and the assumption of Newtonian rheological properties. Very little attention has been given to microfluidic flows involving non-Newtonian working fluids with the notable exception of a microfluidic flow rectifier (and related works) developed by Groisman and co-workers [2, 3]. Their geometry effectively consists of a series of contraction-expansions which are used to generate an irreversible pressure drop that is associated with the motion of a dilute aqueous high molecular weight polymer solution; ie. solutions similar to those used in the present work. Since most fluids processed in lab-on-a-chip devices are likely to exhibit a complex microstructure and exhibit non-Newtonian properties, it is clear that understanding the dynamics of non-Newtonian fluid motion at micron-lengthscales is both fundamentally and practically relevant.

The importance of the geometric scale in micro-hydrodynamics has been of particular question over the past decade. The validity of the continuum assumption at micron-

lengthscales and the influence of surface properties on the effective boundary conditions at the solid-liquid interface have been frequently questioned. As far as the resolution of current diagnostic techniques permits, it has been established that, on micron length-scales, Newtonian fluids essentially obey the fundamental equations governing macro-scale fluid flow in the absence of non-conservative forces (eg. magnetism and electrokinetics) [4, 5]. For geometric lengthscales of l~O(10 μm), the ratio of molecular size/geometry is still 10^{-5}. However, if we consider the mean radius of gyration of a PEO molecule with molecular weight $2\mu 10^6$ g/mol ($R_g \sim N^{1/2}b > 0.16$ μm, where N is the number of Kuhn steps of size, b), the equivalent ratio (under equilibrium conditions) increases by a factor of 1000. If this molecule is extended to its finite extensibility limit, $R_{max} \sim Nb$, this ratio becomes approximately 2. It is therefore not surprising that the geometric scale of microfluidic devices will become increasingly important with non-Newtonian fluids and result in flows (particularly those involving extension) that are different to those seen in the equivalent macro-scale experiment [2, 3]. This is particularly relevant in high speed industrial processes such as roll-coating, electro-spraying/spinning and inkjet printing in which the combination of high velocities and small lengthscales can result in the onset of appreciable elastic effects even in low viscosity aqueous polymer solutions [6].

The Viscoelastic Entry Flow Problem

The non-linear flow phenomena associated with fluid elasticity have been well-studied in macro-scale entry flow. The vortex growth observed in the flow of dilute polymer solutions (η_0 ~ O(1Pa.s) and higher) through abrupt contraction-expansion geometries is extensively documented for axisymmetric [7-10], and to a lesser degree, planar contractions [11-15], for a large number of polymer solutions and polymer melts. Detailed reviews of works published prior to 1987 can be found in [16, 17].

Characterising Entry Flows; Dimensionless Groups

The key dimensionless groups used in characterising entry flows are the Reynolds number, *Re* and the Deborah number *De*. The Reynolds number is defined by $Re = \rho V l / \eta$, in which l is the characteristic lengthscale (which is the contraction diameter in axisymmetric geometries and in planar geometries, is either the contraction width, w_c or the hydraulic diameter, $D_h = 2hw_c/(h+w_c)$), $\bar{V}_c$ is the average velocity in the contraction, and ρ and η are the solution density and viscosity, respectively. The Deborah number is the ratio of two timescales, $De = \lambda/\tau_{flow}$, in which λ is the relaxation time of the fluid and the characteristic timescale in the throat of the contraction, τ_{flow} is the inverse of the local shear rate ($1/\tau_{flow} \sim \dot{\gamma}_c \sim \bar{V}_c/D$). It is also helpful to define an elasticity number, *El* which is the ratio of fluid elasticity to fluid inertia, *El = De/Re.*

In order to assess previous works on viscoelastic entry flows, it is useful to evaluate the flow conditions of each set of experiments in terms of their location in a *De-Re* operating space. The approximate placement of Boger fluids and shear-thinning fluids in *De-Re*

space is presented in Figure 1, which clearly illustrates the effect of shear-rate-dependent material functions associated with shear-thinning fluids. The operating space specific to previous experiments has been summarised in Table 1. Several experiments listed here will be referenced in section 1.1. High-*De*, low-*Re* regions of this operating space are typically accessible using Boger fluids, while regions of moderate *De* and moderate *Re* are characteristic of experiments using semi-dilute or concentrated aqueous solutions of a high molecular weight polymer (such as polyacrylamide (PAA) or polyethylene oxide (PEO)).

One of the difficulties that is faced when comparing previous works on viscoelastic entry flows is selecting meaningful and consistent definitions for the parameters *De*, *Re* and *El*. These are variously defined according to shear-rate-dependent properties (shear-thinning fluids) or as zero-shear-rate properties (Boger fluids). Incorporating the shear-rate-dependent properties of a shear-thinning fluid, results in an elasticity number that decreases with shear-rate and avoids an over-estimation of the appropriate Deborah number which can result in a misleading absence of elastic effects at *De* > 1 [18, 19]. As in the case of [8-10] the viscosity of shear-thinning fluids is frequently described by the power-law relation $\eta(\dot{\gamma}) = K\dot{\gamma}^{n-1}$ and similarly, the first normal stress difference, N_1 is described by a power-law relationship of the form $N_1 = L\dot{\gamma}^m$. The relaxation time is also shear-rate dependent when it is estimated from the ratio of elastic to viscous stresses, such that $\lambda(\dot{\gamma}) = N_1/(2\tau_{yx}\dot{\gamma}) \sim \dot{\gamma}^{m-n-1}$. By using the above power-law relations for $\eta(\dot{\gamma})$ and $\lambda(\dot{\gamma})$, one can obtain a shear-rate dependent elasticity number given by $El = De/Re \sim \dot{\gamma}^{m\text{-}n}/\dot{\gamma}^{2-n} \sim \dot{\gamma}^{m-2}$. In contrast, the elasticity number associated with Boger

fluids ($m > 2$) remains essentially constant at moderate shear-rates. The dependence of the elasticity number on shear-rate is clearly illustrated in Figure 1, in which the trajectories of experiments using shear-thinning fluids have a slope that decreases with increasing Reynolds number and extend into regions of moderate *Re* (a), while those with Boger fluids have high, constant gradients at low shear rates only (b).

To our knowledge, James and Saringer [20] and Groisman and co-workers [2, 3] have published the only experimental investigation of converging flows of dilute polymer solutions at sub-millimetre lengthscales. James and Saringer [20] performed a series of experiments in axisymmetric hyperbolic contractions with minimum exit diameters of approximately 130 microns. The very reason for their choice of lengthscale was to minimise inertial effects at high strains when studying dilute solutions of aqueous PEO (MW = 8×10^6 g/mol) whose concentrations ranged between 5 and 40 ppm ($0.02\ c^* < c < 0.13\ c^*$). Their experiments covered the range, $10 < Re < 300$ and $0.3 < De < 96$, for which they report a number of stable, unstable and rotating vortex flow regimes. The extra pressure drop measurements reported in [20] display features that are attributed to an interplay of elasticity and inertia. The microfluidic flow rectifier developed by Groisman and co-workers [2, 3] was also used to investigate the non-linear dynamical effects observed in dilute aqueous PAA solutions. Their measurements illustrate elastic vortex growth upstream of the contraction plane, and non-linearities in the global pressure drop – flowrate relationship.

1.1 Brief Review of Viscoelastic Entry Flow Phenomena

The work presented here is primarily concerned with flows in planar contractions that are influenced by both inertia and elasticity, so we will therefore focus on contraction flows of moderate values of *Re* and *De*, and also those specific to planar entry flows of dilute polymer solutions. Reference will also be made to numerical simulations of planar flows that incorporate both elasticity and inertia.

The flow structures observed in viscoelastic entry flows have been documented by a handful of authors for planar contractions [11-14, 21, 22], but have been explored more comprehensively for axisymmetric geometries [8-10, 23, 24]. This is especially true for flows that contain both elasticity and inertia. For a clear illustration of the interplay between elasticity and inertia, the reader is referred to the work of Cable and Boger [8-10], who use a number of shear-thinning fluids in axisymmetric contractions to span a wide range of the *De-Re* operating space (Figure 2). Although their work contains both qualitative and quantitative information about the flow structures resulting from both inertia and elasticity, one should be careful when relating these (axisymmetric) phenomena to similar *De-Re* regimes observed in planar geometries, such as those used in the present experiments.

The flow behaviour of inertio-elastic entry flows, such as those in [8-10], can be categorised into three regimes; vortex growth, diverging flow, and unstable flow.

(i) Vortex Growth

The vortex growth behaviour observed in viscoelastic entry flows have predominantly been characterised in terms of a dimensionless vortex length, $\chi_L = L_v / w_u$ (where L_v is the vortex length and w_u is the upstream channel width or diameter), which increases with *De* [24]. In planar entry flows, the principal effect of the geometric change is to reduce the size of the salient corner vortex for the same contraction ratio. An argument for this behaviour is that the total Hencky strain imposed on the polymer molecules during the converging flow reduces with the change from uniaxial to planar kinematics [25]. This is supported by the results of Nigen and Walters [15] in which the authors give a direct comparison of the same Boger fluid in planar and axisymmetric contractions of the same contraction ratio. This suggests that the extension rate (and thus *De*) is not the only parameter to be considered in entry flows, especially when comparing axisymmetric to planar geometries. In addition to the reduced Hencky strain, there are also three-dimensional flow effects due to the finite depth of the channel. This latter effect is likely to result in discrepancies when comparing flows in planar geometries with the results of 2D numerical simulations.

This geometric influence on the vortex size is also modulated by the solution rheology. For example, in the case of Boger fluids, elastic vortex growth is suppressed to the point at which vortices do not grow at all [15]. On the other hand, shear-thinning fluids which do not have a large background solvent viscosity exhibit vortex growth [11-15, 26], although the degree of vortex growth is still somewhat reduced when compared with axisymmetric geometries [27].

Several authors have been able to successfully predict the vortex growth (including both lip and vortex features) for shear-thinning fluids in both planar [28] and square contractions [29]. Vortex growth is not observed in numerical simulations for UCM or Oldroyd-B fluids in planar contractions [30-33] for $De \leq 2$, which agrees with the experimental results of [15]. However for $2 < De < 8$, mild vortex growth has been predicted in planar contractions for a UCM fluid [34].

Inertia also has an effect on vortex development. In the case of inertio-elastic flows, the vortex growth is truncated at a critical Reynolds number, Re_{crit}, which depends on the elasticity of the fluid. For $Re < Re_{crit}$, vortex growth is dependent only on the rheology of the fluid, while for $Re > Re_{crit}$, inertia causes a reduction in vortex size, which is accompanied by *diverging flow* patterns [10]. This phenomenon is most frequently observed in shear-thinning fluids, however it has also been seen in constant viscosity elastic fluids at low Reynolds numbers ($Re \sim O(0.01)$), both experimentally in axisymmetric contractions [35] and numerically in planar contractions [34]. Alves [29] found that the vortices in a PAA Boger fluid were almost completely suppressed for Reynolds numbers as low as $Re > 0.2$, far lower than the equivalent value of the critical Reynolds number for the Newtonian fluid ($Re > 7$). This "inertial suppression" was accompanied by diverging streamlines (a hallmark of fluid elasticity), which continue for increasing Re and De and remain present during vortex growth at sufficiently high Deborah numbers. A similar observation was also made experimentally by Boger and Binnington [7], and has also been numerically predicted by Xue and co-workers [36] for

an Oldroyd-B fluid over the range $0.06 < \mathrm{Re} < 0.62$ (and constant $De = 1.6$) in three-dimensional planar geometries. For all Reynolds numbers in this range, the vortex size was smaller for the Oldroyd-B fluid than for a Newtonian fluid. These results mentioned heretofore demonstrate that both dimensionless variables, *Re* and *De* are independently important in assessing the vortex growth behaviour and influence of inertia.

(ii) Diverging Flows

Diverging streamlines are a feature of converging flows that experience both elasticity and inertia. A comprehensive illustration of this flow regime is detailed in work of Cable and Boger [10]. Diverging flow is usually seen in shear-thinning fluids, since it is easier to generate moderate values of *Re*, however flow patterns in the early stages of this regime have been observed in the circular entry flow of Boger fluids, at Reynolds numbers as low as 0.9 [7].

Features of diverging flow have also been predicted numerically in the presence of both elasticity and inertia, for shear-thinning fluids represented by the PTT [37] or FENE-P [28] models. At a constant value of *Re* for which inertia is important, increasing *De* may either strengthen or weaken diverging flow depending on the elasticity number and/or the contraction ratio.

(iii) Unstable Flow

Unstable viscoelastic flow is observed at moderate Deborah and Reynolds numbers in axisymmetric and planar geometries however the nature of the streamlines is highly

dependent on the elasticity of the solution and the geometry. The spatio-temporal characteristics of these unstable flow regimes have been found to be dependent on the elasticity number. For an axisymmetric geometry, it has been found that lower elasticity solutions experience regimes consisting of diverging flow with unstable salient vortices, and regimes with Goertler-like and lip vortices, while for higher elasticity solutions, unstable regimes extend to asymmetric flow patterns, azimuthally varying salient vortices, and 'buckling' flow structures. The "Goertler-like" vortex regime is also common to 4:1 planar contractions of high aspect ratio, $h/w_c > 20$ using the same low elasticity solutions [13, 14].

(iv) Pressure drop

The extra pressure drop above that which would be measured in the equivalent Newtonian experiment is used as a measure of the "apparent" extensional viscosity of polymer solutions. The pressure drop over the entrance region has been measured in Boger fluids in both axisymmetric [25] and planar contractions [15]. Rothstein and McKinley [25] measure a dimensionless pressure drop of $1 < \Delta P < 4$, for a polystyrene Boger fluid and contraction ratio, $\beta = 4$. Similar results ($1 < \Delta P < 2$) have also been observed by Nigen and Walters [15], for their polyacrylamide Boger fluids in a 4:1 axisymmetric contraction. However, in planar contractions, they observed no appreciable difference between the pressure drops for the Boger and Newtonian fluid.

Currently, the only existing pressure drop measurements for aqueous polymeric solutions are those of James and Saringer [20] and Groisman and Quake [3]. James and Saringer

[20] measure a dimensionless pressure drop greater than unity which occurs beyond a critical strain rate, and is influenced by both the polymer concentration and Reynolds number; however because of the choice of fluid, these two variables are inseparable. Groisman and Quake [3] measure the pressure drop of both the forward and reverse flow of a dilute polyacrylamide aqueous solution through a saw-tooth geometry over a range of Deborah and Reynolds numbers, $0.4 < De < 19$ and $0.22 < Re < 11$. They measure a dimensionless pressure drop, $\Delta P \geq 1$ for $De \geq 2$ and $Re \geq 1$, which increases to a maximum value of $\Delta P > 6.7$ at $De > 5.2$, $Re > 3$.

In the present work, we investigate the flow of dilute and semi-dilute polyethylene oxide (PEO) solutions ($1.3 < c/c^* < 4$) through micro-fabricated planar abrupt contraction-expansions of contraction ratio, $\beta = 16$. Experiments are performed over a range of Deborah and Reynolds numbers ($27 < De < 548$, $0.44 < Re < 64$), in a region of *Re-De* parameter space that has previously been unexplored as illustrated in Figure 2. We investigate the competing effects of inertia and elasticity on vortex growth and the structure of flow instabilities in the micro-contraction flows. Video-microscopy and streak imaging with 1.1 micron diameter epifluorescent seed particles are used to characterize the steady flow kinematics upstream of the contraction for both a Newtonian fluid and three aqueous polyethylene oxide solutions. The pressure drop is measured over a section of the channel containing the abrupt contraction-expansion, in order to quantify the extra pressure drop due to the elasticity of each of the solutions. The inverse dependence of the elasticity number on the length-scale of the geometry makes it possible to attain high values of *De* and *El* using semi-dilute aqueous polymer solutions in

microfluidic devices; conditions not typically accessible in the equivalent macro-scale experiment.

2.0 EXPERIMENTAL

2.1 Channel Geometry and Fabrication

In Figure 3, we illustrate the dimensions of the 16:1:16 planar abrupt contraction-expansion with an upstream channel width, w_u = 400 μm, downstream contraction width, w_c = 25 μm, contraction length, L_c = 100 μm, and uniform depth, h = 50 μm. The detachment point of the salient corner vortex L_v is used to define the dimensionless vortex length $\chi_L = L_v / w_u$. Channels were fabricated in polydimethylsiloxane (PDMS) using soft-lithography and SU-8 photoresist molds (Microchem NANO ™ Su-8-50, www.microchem.com) which were fabricated using stardard photo-lithographic procedures [38, 39]. The SU-8 molds were fabricated using a high-resolution chrome mask (Advance Reproductions, www.advancerepro.com) together with a contrast enhancer (Shin-Etsu MicroSi CEM 388SS, www.microsi.com) and barrier coat (Shin-Etsu MicroSi CEM BC 7.5). Contrast enhancer is an opaque photo-bleachable material, whose exposed regions become more transparent over time. It is applied between the mask and photoresist to effectively absorb low intensity light (refracted light) while transmitting direct light in open regions through to the photo-resist. This results in sharp features at the contraction entrance and near-vertical channel walls along the entire length of the channel as illustrated in Figure 4 (a) - (c). PDMS channels and microscope coverslips (170 μm thickness) are air-plasma treated (75W, 700 mTorr) for approximately 40 seconds and brought into contact to achieve a covalently bonded

interface that is resistant to high pressures. Further details of the channel design and fabrication procedure are found elsewhere [40].

Pressure taps were integrated into the device at axial locations 6 mm upstream (15 upstream channel widths) and downstream of the contraction plane, in order to measure the differential pressure drop, ΔP_{12} as a function of flowrate for each of the polymer solutions and for the Newtonian fluid. Inlet and outlet ports for connection to a constant displacement-rate syringe pump (Harvard Apparatus PHD2000) were located an additional 6 mm upstream and downstream of the pressure taps. Volumetric flowrates spanning the range $0.1 \leq Q \leq 18$ ml/hr were used in the present experiments. This gives characteristic deformation rates $1800 < \dot{\gamma} = 2\overline{V}_c / w_c < 3.2 \times 10^5 s^{-1}$.

2.2 Fluid Rheology

Three aqueous solutions containing 0.05%, 0.10% and 0.30% polyethylene oxide (PEO; 2×10^6 g/mol) were used in this work. For brevity, we denote these compositions by 0.05%, 0.1% and 0.3%, respectively. The rheological properties of these solutions are given in Table 2. The characteristic relaxation times reported in the table were measured using capillary breakup extensional rheometry (CaBER) [41], and have a range of $0.7 < \lambda < 4.4$ ms. Using this method, reproducible and reliable measurements of the relaxation time of these semi-dilute, low viscosity solutions can be obtained, but show a weak dependence on the geometric configuration of the CaBER instrument [41]. Following the nomenclature of [41], an aspect ratio of $\Lambda = 1.6$ and an initial gap height of 2.7 mm ensured maximum reproducibility.

All measured values of the relaxation time were greater than those predicted according to Zimm theory, in which the relaxation time is given by [42]:

$$\lambda_{\text{Zimm}} = F\frac{[\eta]M_{\text{W}}\eta_{\text{s}}}{N_{\text{A}}k_{\text{B}}T} \tag{1}$$

Here, M_{W} is the molecular weight, N_{A} is Avogadro's constant, k_{B} is Boltzmann's constant, T is the absolute temperature, η_s is the solvent viscosity, and $[\eta]$ is the intrinsic viscosity given by the Mark-Houwink relation; for PEO this has been determined experimentally to be $[\eta] = 0.072\,M_{\text{W}}^{0.65}$ by Tirtaatmadja et al. [42]. This gives $[\eta]$ = 897 ml/g for a molecular weight of 2 μ 10^6 g/mol. The prefactor, F is given by the Riemann Zeta function, $\zeta(3\nu)^{-1} = \sum_{i=1}^{\infty} 1/i^{3\nu}$ in which ν is the solvent quality exponent which is calculated from the exponent $a' = 3\nu - 1$ in the Mark-Houwink relation. For PEO, $a' = 0.65$ [42] and hence ν = 0.55. The overlap concentration, c^* is calculated according to the expression of Graessley [43], which gives c^* = 0.77/$[\eta]$ = 858 ppm for these solutions. With a front factor $F = \zeta(1.55)^{-1}$ = 0.463, we calculate a Zimm time of λ_{Zimm} = 0.341 ms, significantly lower than the measured relaxation time, λ = 1.2 ms, for the 0.05% PEO solution (c/c*= 500/858 = 0.58). As the polymer concentration increases, the relaxation time determined from capillary breakup measurements also increases. Similar trends have been documented in other capillary breakup experiments [44, 45]. The concentration dependence of the shear rheology of numererous aquous polymer solutions has also been investigated in detail by Tam and Tiu [46].

The steady shear viscosities of the solutions used in the present study were determined using a controlled stress rheometer (AR2000) with a double gap Couette cell at shear rates, $1 \leq \dot{\gamma} \leq 10^4$ s^{-1} with zero-shear rate viscosities ranging between $1.8 < \eta_0 < 8.3$ mPa.s. The shear viscosity for each fluid, as a function of shear rate, is shown in Figure 5. All three solutions were found to be mildly shear-thinning at high deformation rates, exhibiting power law behaviour. Approximate power-law constants for each of the fluids are also given in Table 2.

The upper limit on the data is constrained by the onset of a flow instability. This is manifested as an apparent increase in viscosity at high shear rates, and can be predicted according to a linear stability analysis [47]. For a Newtonian fluid the onset of inertial instabilities is given by:

$$Ta_{\text{crit}} \equiv 2Re^2\varepsilon = 3400 \tag{2}$$

in which Re is the Reynolds number and $\varepsilon = d/R_1$, d is the gap width and R_1 is the radius of the inner cylinder. The Reynolds number is defined as $Re = \Omega_1 R_1 d\rho / \eta(\dot{\gamma})$, in which Ω_1 is the angular rotation of the inner cylinder, ρ is the density of the fluid and $\eta(\dot{\gamma})$ is the shear-dependent viscosity. Substituting this expression into equation 2, and using values R_1=22 mm, d = 0.38 mm, ρ > 1000kg/m^3, the criterion for onset of inertia instability can be rearranged in the following form:

$$\eta(\dot{\gamma}) = 5.02 \times 10^{-7}\dot{\gamma} \tag{3}$$

with η in Pa.s and $\dot{\gamma}$ in s^{-1}. This equation is represented by the dashed line in Figure 5 and is in reasonable agreement with the data. If we apply the criterion for a purely elastic

instability, given by $[\varepsilon^{1/2} Wi]_{\text{crit}} = 5.92$ [47] where $Wi_{crit} = \lambda \dot{\gamma}_{\text{crit}}$ and $\dot{\gamma}_{\text{crit}}$ is determined experimentally from Figure 5, the longest relaxation time would increase ($3.6 < \lambda < 9.7$ ms) with decreasing concentration (for the same solvent viscosity). The source of the instability observed at high shear rates in Figure 5, is therefore attributed to inertial instabilities.

The low shear-rate limit of the viscometric data is determined by the minimum torque associated with the instrument, which is given by the manufacturer as $\Im_{\text{min}} = 10^{-7}$ N.m [48]. Using the applicable geometric factor and stress factors for the double-gap Couette cell, the minimum shear stress measurable by the instrument is given by $(\eta\dot{\gamma})_{\text{min}} = F_{\text{DC}}\Im_{\text{min}}$, which is equivalent to the inequality $\eta \geq F_{\text{DC}}\Im_{\text{min}} / \dot{\gamma}$, with $F_{\text{DC}} = 2976$ m^{-3} given on the lower left-hand corner of Figure 5.

Due to the low viscosity of these solutions, small amplitude oscillatory shear measurements of the elastic storage modulus $G'(\omega)$ could not be performed successfully and as a result, we could only evaluate the longest relaxation time, λ through capillary breakup experiments. At the lowest concentration (500 ppm) even capillary thinning and breakup experiments become difficult to resolve. The thread thins and breaks within 20 – 40 ms. The mean value of the time constant obtained from repeated experiments was $\bar{\lambda}_{0.05} = 1.2$ ms. The relaxation time for the 0.05% PEO solution, used in computing *De* has been adjusted from this experimentally measured value. Essentially, the relaxation time has been adjusted downwards to λ = 0.7ms so that the onset of inertio-elastic instabilities occurs at the same *De* for all three solutions. The 0.1% and 0.3% PEO

solutions were already in agreement with respect to a critical Deborah number $De_{crit} > 50$ for the onset of elastic instabilities. Flow visualisation studies showed that the onset of elastic instabilities for the 0.05% PEO solution occurred at higher deformation rates corresponding to a markedly higher critical Deborah number if we chose λ = 1.2ms. It has therefore been deduced that the real relaxation time of the 0.05% PEO solution is below the lower measurable limit of our current capillary breakup apparatus. One possible choice of presentation would be simply to report dimensional values of the critical shear rates observed in the 0.05% solution. However to be consistent with our presentation of results for the 0.1 and 0.3% fluids we have instead chosen to adjust the relaxation time by a constant factor of $(De_{crit})_{0.1,\,0.3}/(De_{crit})_{0.05}$ = 50/85 = 0.58, resulting in a value of $\lambda = 0.58\text{l} \times 1.2$ ms = 0.7 ms. This adjustment results in the onset of elastic instabilities in the planar contractions occuring at the same value of De_{crit} = 50 for all solutions.

2.3 Flow Visualisation

The fluids are seeded with 1.1 μm diameter fluorescent particles (Ex/Em = 520/580 nm) at a concentration of 0.02% wt. For neutrally buoyant particles, this corresponds to a volume fraction of $\phi = 2 \times 10^{-4}$, for which we expect a negligible increase in viscosity according to the Einstein expression $\eta = \eta_0 \{1 + 2.5\phi\} = 1.0005\eta_0$. In Figure 6 we show the optical set-up for the streak imaging experiments. A 10X 0.3NA objective lens is used in conjunction with a full-field continuous illumination mercury lamp at 532 nm.

The corresponding DOF is given by:

$$\delta z = \frac{n\lambda_0}{NA^2} + \frac{ne}{NA\,M} \tag{4}$$

provided $e/M > d_p$. In the above equation, M is the magnification, and e is the smallest resolvable distance by the detector in the image plane. For our system, δz = 3.4 μm.

Although the depth of field (DOF) of the imaging system itself is only 3.4 μm, this is misrepresentative of the true depth of the image plane on which streak lines are observed. The true 'depth of measurement' is calculated according to the theory of [49], who originally developed the analysis for calculating the measurement depth, δz_m in particle image velocimetry. The depth of measurement is given by:

$$\delta z_m = \frac{3n\lambda_0}{(NA)^2} + 2.16\frac{d_p}{\tan\theta} + d_p \tag{5}$$

in which, NA is the numerical aperture of the lens, n is the refractive index of the medium being imaged, λ_0 is the wavelength of light in a vacuum, d_p is the particle diameter, and $\theta = \sin^{-1}(NA/n)$. In this expression, the three terms on the right hand side of the equation, from left to right, represent the components associated with diffraction, geometrical shadow and the size of the particle. For our particular optical setup, δz_m = 29.7 μm, and thus corresponds to 60% of the depth of the channel. It is expected that this value is a better estimate of the depth over which particles contribute to the observable streak lines than using the DOF, which only accounts for *in focus* streamlines.

Streak images are acquired on a 3.5 MP Apogee CCD camera (2184 × 1472 pixels) with a 30ms exposure time. The transient behaviour (ie. start-up, shut-down and fully-developed unstable flow regimes) of the flow in the micro-contraction was also captured using a Pulnix CCD camera (768 × 494) at a frame rate of 29.97 fps and exposure time of 16 ms, although sequences from these movies have not been included in this paper. They are provided as supporting material online (http://web.mit.edu/lerodd/www).

2.4 Pressure Drop Measurements

Pressure measurements are taken via two pressure taps which are located upstream and downstream of the contraction plane, as depicted in Figure 6. The two pressure taps (stainless steel tubing, OD = 0.71mm) are connected via 0.7mm ID flexible Tygon tubing to a Honeywell 26PC differential pressure sensor. Three pressure sensors were used to cover a differential pressure range of $0 < \Delta P_{12} < 200$ kPa. The voltage output of each of the sensors was calibrated for the differential pressure range $0 < \Delta P_{12} < 30$ kPa using a static column of water. For higher pressures, the sensors were calibrated using a pressurised nitrogen line and independently calibrated digital pressure gauge. The calibration curves for each of the pressure sensors are given in Figure 7(a).

In each of the steady state experiments, the transient pressure was recorded for a duration of approximately 3-5 mins after the inception of flow (or step increase in flowrate). The flow rate was increased incrementally, to achieve a range of steady state pressure drops corresponding to flowrates, $0.1 < Q < 18$ml/hr. The transient response associated with each of these step increases in flowrate, are illustrated in Figure 7(b). The response time of the system is much longer than the relaxation time of the polymer of any convective time scale of the flow and is expected to be weakly dependent on the deformability of the fluid channel and compressibility in the pressure tap tubing, resulting from small amounts of trapped air. However, it is predominantly dependent on the angular velocity of the syringe pump gearing. Small volume syringes, which use higher rotation speeds for the same flowrate, require less time to reach a steady state pressure measurement. This is

consistent with the analysis of Dealy [50] for weakly compressible flows of polymer melts from reservoirs. The steady periodic modulation of the pressure drop measurement about the mean steady state value can be seen in Figure 7b. and is also dependent on the rotation rate of the syringe pump. The pressure drop for each flowrate is taken as the mean steady state value of these oscillations.

2.5 Dimensionless Parameters

The dynamics of the flow through the micro-scale geometries are characterized by the following dimensionless quantities: Deborah number (*De*), Reynolds number (*Re*) and elasticity number (*El*) which are defined according to Equations 6 - 8. The Deborah number is defined in terms of the average shear rate, $\dot{\gamma}_c$ in the contraction throat:

$$De = \lambda \dot{\gamma}_c = \frac{\lambda \bar{V}_c}{w_c/2} = \frac{\lambda Q}{h w_c^2/2} \tag{6}$$

where λ is the relaxation time of the fluid, $\bar{V}_c = Q/(w_c h)$ is the average velocity, w_c is the contraction width, h is the depth of the channel and Q is the volumetric flowrate. The Reynolds number is

$$\mathrm{Re} = \frac{\rho \bar{V}_c D_h}{\eta_0} = \frac{2\rho Q}{(w_c + h)\eta_0} \tag{7}$$

where ρ is the fluid density, η_0 is the zero shear viscosity and the hydraulic diameter is given by $D_h = 2w_c h/(w_c + h)$. Finally, the elasticity number is

$$El = \frac{De}{Re} = \frac{\lambda \eta}{\rho w_c D_h} = \frac{\lambda \eta (w_c + h)}{2\rho w_c^2 h} \tag{8}$$

As we have noted in the introduction, the elasticity number, *El* is dependent only on fluid properties and the inverse square of the characteristic length-scale of the channel. It is constant for a given fluid and geometry, ie. *El* is independent of the kinematics of the flow. In the present experiments, the elasticity numbers are *El* = 3.8, *El* = 8.4, and *El* = 89 for the 0.05%, 0.1% and 0.3% PEO solutions, respectively. It may be noted from equations (6) and (7), that *De* and *Re* are defined according to zero-shear rate properties. For cases in which the geometry is kept the same (ie. the product $w_c D_h$ is held constant), a variation in *El* is a direct measure of the variation of the elasticity of the fluid, provided the relaxation time and viscosity are not rate-dependent. Although it is customary to characterise the shear-thinning effects in entry flows by reporting the shear-rate dependent rheological properties of the test fluids, it was not possible to measure the steady shear viscosity over the full range of shear rates used in the experiments $2000 < 2\times10^3 < \dot{\gamma} < 3.2\times10^5 s^{-1}$ (see Figure 5). In addition, it was not possible to obtain normal stress data for these fluids, leaving the (constant) relaxation time determined from capillary breakup experiments as the only directly measurable timescale for the fluid. As we have seen, these values are substantially higher than the value λ_Z that may be inferred from the intrinsic viscosity and molecular weight information. As a result, the computed values of *De* and *Re* increase linearly with shear rate and the range of *De* and *Re* that can be accessed is unbounded. We may contrast this with the response obtained from a more-realistic nonlinear viscoelastic constitutive equation such as the PTT or Giesekus models in which the material functions exhibit a rate-progressive thinning. For simplicity, we consider here a hypothetical viscoelastic fluid in which the viscometric properties are

given by power law functions, $\eta = K\dot{\gamma}^{n-1}$, $N_1 = L\dot{\gamma}^{m}$. A Maxwellian relaxation time may be defined as:

$$\lambda(\dot{\gamma}) = \frac{\Psi_1(\dot{\gamma})}{2\eta(\dot{\gamma})} = \frac{N_1(\dot{\gamma})/\dot{\gamma}^2}{2\eta(\dot{\gamma})} = \left(\frac{L}{2K}\right)\dot{\gamma}^{m-n-1} \tag{9}$$

and the elasticity number consequently varies as $El \sim \eta\lambda \sim \dot{\gamma}^{m-2}$. At low shear rates, $\dot{\gamma} \ll 1/\lambda$, $m \to 2$ and the elasticity number is constant. However at high deformation rates, $\dot{\gamma} \gg 1/\lambda$, it is common to observe for many polymeric fluids that $m \cong 2n \leq 2$ [51]. The effective relaxation time decreases and the Deborah number increases with deformation rate more slowly than the Reynolds number. This may be seen very clearly in the data plotted in *De-Re* space in Figure 2. Similar ideas are discussed by Stokes et al. [52] when examining another complex viscoelastic flow; the swirling motion of dilute and semi-dilute polymer solutions. The importance of this difference between rate-dependent and rate-independent material functions for numerical simulations has also been discussed at length by Boger et al. [19]. For clarity, we therefore follow the approach of Rothestein and McKinley [25] and report our flow parameters in terms of the zero-shear-rate material properties. The appropriate volumetric flow rate (Q) or the deformation rate in the contraction $(\dot{\gamma}_c)$ to be used in numerical simulations can then be found directly from equations (6)-(8).

The dimensionless vortex length, $\chi_L = L_v/w_u$ is defined according to the convention in previous macro-scale entry flow experiments [16], to quantify the axial distance upstream from the contraction plane, at which the primary flow first detaches from the channel wall.

In computational studies of viscoelastic flow through contractions it is customary to report the Couette correction $C = \Delta P_{en} / 2\tau_w$ [30], in which ΔP_{en} is the pressure drop across the entrance plane and τ_w is the wall shear stress in the contraction. In experiments however it is a global pressure drop across the entire geometry ΔP_{12} that is most readily measured by macroscopic pressure transducers located at points '1' and '2'. In the case of axisymmetric flows with constant viscosity boger fluids it is possible to subtract the contribution to the overall pressure drop that arises from the fully developed pipe flow upstream and downstream of the contraction [25, 53]. However, the three-dimensional nature of the flow in rectangular microfluidici channels, coupled with shear-thinning in the fluid rheology at high shear rates makes this impractical. We therefore report the total pressure drop ΔP_{12} between the two transducers (located 6 mm upstream and downstream of the contraction plane). The dimensionless pressure, ΔP is obtained by normalising the differential pressure ΔP_{12} by the linear slope of the pressure drop/flowrate curve that is observed in all experiments at low *De* [15], such that $\Delta P(Re,De) = \Delta P_{12}/(sQ)$, where $s = \Delta P_{12}/dQ$ when $Q \rightarrow 0$.

3.0 RESULTS

We begin by comparing the flow patterns observed in the micro-contraction observed with those obtained using Newtonian fluids. We then systematically compare the vortex size, fluid streamlines and flow stability in each of the three viscoelastic fluids as a function of increasing shear rate. Finally we quantify the dimensionless vortex size and the associated increase in the pressure drop resulting from the contraction flow.

3.1 The Effect of Elasticity

In Figure 8 we illustrate a well-known feature of non-Newtonian flows, in which elasticity has the *opposite* effect to inertia [54]. This has been demonstrated previously in experiments with xanthan gum solutions and aqueous polyacrylamide solutions in macro-scale contraction-expansion geometries [55]. Similar trends have also been simulated in narrow 'slit-like' planar contraction geometries by Baloch et al. [37]. Here we compare the flow of the 0.05% PEO solution (Figure 8 (a)) in which the effects of both elasticity and inertia affect the flows, with the flow of water (Figure 8 (b)) at the same value of Re. At low flowrates ($Re > 5$), the streak lines appear visually identical in both (a) ($Q_{El=3.8}$ = 1.25 ml/hr) and (b) ($Q_{El=0}$ = 0.5 ml/hr). In the Newtonian case (Figure 8 (b)), an increase in Reynolds number to $Re = 11$ ($Q_{El=0}$ = 1.5 ml/hr), results in a barely perceptible flattening of streamlines on the upstream side of the contraction plane, and the formation of a pair of "lip vortices" on the downstream side. These vortices first appear for $Re \geq 11$, and continue to grow until $Re > 20$ ($Q_{El=0} > 2.75$ ml/hr), at which

point these isolated 'lip vortices' grow into the stagnant downstream corner as shown in Figure 8 (b). The downstream corner vortices continue to grow and extend downstream in a symmetric fashion for the entire range of flowrates tested up to Re = 60 ($Q_{El=0}$ = 8 ml/hr). This is higher than the predicted onset of a symmetry-breaking bifurcation, which is expected for $Re \geq 54$ according to the two-dimensional simulations of Newtonian planar expansion flows. The onset of this bifurcation has been predicted for the same critical Reynolds number by several other authors using a range of techniques [56-59]. Three dimensional effects may serve to stabilize the flow against symmetry breaking

Streak line analysis showed that the flow appeared to be stable over the entire range of flowrates tested, $0.15 < Re < 60$. The images at Re = 18 and 29 ($Q_{El=0}$ = 2.5 and 5 ml/hr) are similar to those observed by Townsend and Walters in their macro-scale 14:1 planar expansion geometry. Small quantitative discrepancies arise as a result of difference in contraction ratio and the use of a square cross-section contraction throat in the work of [55], as compared with our geometry which has an aspect ratio (contraction channel width/depth) of w_c/h = 0.5. Rescaling our own values of Re according to the contraction width instead of hydraulic diameter yields a modified Reynolds number $\tilde{R}e = \rho \bar{V}_c w_c / \eta$ = 27, which is in good agreement with [22]. This emphasises the importance of choosing appropriate definitions of dimensionless parameters when seeking to make quantitative comparisons with previous studies.

It should be noted that in Figure 8, the length of the contraction used for the Newtonian fluid experiments (L_c = 200μm) is longer than the length of the contraction in the

experiments using the 0.05% PEO solutions (L_c = 100μm). The streaklines that are observed in the viscous Newtonian fluid downstream of the contraction plane are fully developed and independent of contraction length. By this argument, so long as L_c is kept constant for all experiments with each of the non-Newtonian fluids (in which fluid memory *is* important), it does not matter what value of L_c is chosen for the Newtonian fluid (which has *zero* fluid memory). This is the case *only* for streakline analyses, and a constant L_c = 100 μm has been used for all pressure drop experiments.

In the case of the 0.05% PEO solution (El = 3.8), the effects of fluid elasticity are to suppress the formation of downstream vortices for all flowrates. Only at $Re \geq 50$, are the inertial effects great enough to support downstream vortex growth (Re = 56, De = 212, Q = 14ml/hr). Upstream of the contraction, Newtonian-like behaviour is observed up to $De > 60$, at which point the streak lines begin to show significant viscoelastic bending in the entrance region ($-2w_c \leq z \leq 0$). Inertial effects lead to a complete collapse of the salient corner vortex in the upstream corners.

This transition between the bending streamlines and vortex growth regimes is depicted more clearly in Figure 9 for the 0.05% PEO solution. Analysis of the streaklines of the 0.05% PEO solution indicate that the flow is stable at Re = 18, De = 68. For $19 \leq Re \leq 23$, $72 \leq De \leq 87$ the flow becomes inertio-elastically unstable and unsteady in nature. The apparent crossing of streamlines is partly an artefact of the depth of the imaging plane (section 2.3) but indicates that the flow upstream of the throat is also three-dimensional. At sufficiently high Reynolds numbers and Deborah numbers, $Re \geq$

24, $De \geq 91$, a large viscoelastic corner vortex forms abruptly, and is bistable; ie. the vortex may rapidly jump from being initially attached to the 'lower' surface of the upstream contraction (as observed in the microscope images) to then being attached to the 'upper' surface as shown in Figure 9 at $Re = 24$. Additional experiments showed that there is hysteresis during this flow transition. On slowly decreasing the flow rate, the streaklines collapse back to the form shown in the third frame of Figure 9, however at lower values of Re and De. The precise shape of the hysteresis curve on an $\chi_L - De$ diagram remains to be quantified. At higher flowrates, asymmetric vortices continue to grow upstream for $24 < Re < 72$ and $91 < De < 272$.

3.2 The Effect of Increasing Elasticity; *El* = 3.8, 8.4, and 89

In Figure 10, we illustrate the evolution of the upstream flow structure prior to the formation of the elastic corner vortex in three solutions of varying elasticity; 0.05% PEO ($El = 3.8$), 0.1% PEO ($El = 8.4$) and 0.3% PEO ($El = 89$). In both Figure 10 and Figure 11, each column documents the sequence of streak lines associated with a single solution as the flowrate is progressively increased. The three images in each row illustrate the streak lines at approximately the same value of De for each solution, but with varying degrees of inertia. The onset of unstable flow occurs at $De_{crit} > 50$, at which point the smoothly converging streamlines are replaced by 'wine-glass' – shaped streamlines, which is particularly clear in the 0.05% PEO solution. At a slightly higher Deborah number, $De > 67$ ($Re = 7.8$), the 0.1% PEO solution undergoes an inertio-elastic instability immediately upstream of the contraction plane. Further reducing the Reynolds

number at a constant Deborah number (0.3% PEO) results in instabilities that are similar in nature and confined to the core region around the contraction entrance, however the streaklines are more coherent and show less pronounced inertial fluctuations.

At $De > 80$ and $Re \geq 9$, inertio-elastic instabilities extend into the upstream corners of the contraction and envelop a large part of the entrance region ($-5w_c \leq z \leq 0$). In contrast, the more elastic 0.3% PEO solution ($De = 78$, $Re = 0.87$) develops a small quasi-stable lip vortex. For all three solutions, the inertio-elastic instabilities are ultimately replaced by quasi-stable upstream corner vortices for $120 < De < 270$. These vortices are stable, such that the mean value of the vortex length $\bar{L}_v$ has a well-defined constant value over time, although the instantaneous value oscillates around $\bar{L}_v$ with a frequency that depends on the speed of the flow. The oscillations in vortex size for the 0.3% PEO solution appear to be more pronounced, particularly for $De > 120$. As the Deborah number is increased further, the large elastic vortices grow upstream in all cases, however the transient dynamics associated with establishing a stable vortex position varies systematically from one fluid to another. For the least elastic solution (0.05% PEO), the flow remains asymmetric for all values of De attained. For $120 < De < 170$, the upstream corner vortices continue to grow in size, however their orientation periodically switches from 'upper' to 'lower' surfaces. Eventually, for $De \geq 180$, vortices form in both upstream corners, although unequal in size.

The 0.1% PEO solution displays similar behaviour, although a quasi-stable, top-bottom symmetric flow pattern is achieved at a much lower Deborah number ($100 < De < 120$).

In conjunction with this development, a "diverging flow" regime develops upstream of the elastic corner vortices, and is clearly evident at De = 240. As we discussed in the introduction this local diverging flow appears to be a hallmark of contraction flows in which viscoelasticity, inertia and deformation rate-dependent material functions are all important. The flow patterns of the 0.05% PEO solution upstream of the contraction at De = 272 can also be characterised as "diverging", although this divergence is skewed by the asymmetry of the flow. The 0.3% PEO solution displays vortex growth of the same order of magnitude, although the flow asymmetry is greatly exaggerated at high De.

Another noticeable feature in all fluids at high De is the hyperbolic shape of the dividing streamlines that separate the recirculating corner flow from the main converging flow upstream of the contraction. The fluid appears to converge more rapidly in the case of the 0.1% PEO, with a much narrower width at the exit of the hyperbola that is approximately half the size measured for the 0.3% PEO solution.

3.3 Evolution in Vortex Length

The streak images present in sections 3.1 and 3.2 have shown that there are significant changes in the vortex activity both upstream and downstream of the contraction plane with increasing flowrate. In Figure 12, we quantify the vortex growth for all three solutions. Data for all three solutions collapse onto the same curve which represents an almost-linear relationship between dimensionless vortex length and *De*, although the slope appears to lessen at high *De.*

The effect of inertia is to reduce the size of the upstream corner vortex, and this can be seen most clearly in cases for which elasticity is not important. In the current work, the dimensionless vortex length decreases to a minimum value of $\chi_L = 0.1$, which is half the predicted value for creeping flow of a Newtonian fluid through a planar contraction. The Newtonian prediction was made by [60] using a finite volume method for a PTT fluid with $De = 0$, in contraction ratios of 10, 20, 40 and 100. For contraction ratios, $\beta \geq 10$, the vortex length was found to be constant and equal to $\chi_L = 0.2$. For the 0.3% PEO solution, in which a minimum Reynolds number of 0.5 was achieved, the minimum vortex length was 0.18, substantially closer to the creeping flow prediction. At higher Reynolds numbers, $Re \geq 0.5$, the vortex length increased linearly with flowrate, however substantial scatter was observed in the χ_L – De data for $50 \leq De \leq 150$.

On the basis of the streakline analyses, viscoelasticity does not seem to be important in these low-inertia flows for all three solutions, although the corresponding values of the

Deborah numbers at these low flowrates were De = 7.6 and De = 40 for the 0.05% PEO and 0.3% PEO solutions respectively. The onset of substantial vortex growth occurred at De > 110, even though the onset of inertio-elastic instabilities occurred at De_{crit} > 50. The onset of significant elastic vortex growth is also associated with the three-dimensional character of the flow field upstream of the contraction, and is therefore likely to be dependent on the aspect ratio of the channel, $\Lambda = w_c/h$. Care must be taken when making qualitative comparisons between the value of Deborah numbers reported here and those of previous studies. The values of De in the present work are based on a constant relaxation time, and are therefore an upper bound because reduction of the viscometric properties with shear-rate associated with shear-thinning fluids will lead to a decrease in relaxation time and thereby reduce the effective level of elasticity in the flow. The values of De_{crit} correspond to a shear-rates of 59 μ 10^3 s^{-1}, 33 μ 10^3 s^{-1}, and 11 μ 10^3 s^{-1} for the 0.05%, 0.1% and 0.3% PEO solutions, respectively. Consideration of Figure 5, shows that these shear rates correspond to the shear-thinning region for each of the solutions, particularly for the 0.3% PEO solution. In addition, the Reynolds number reported herein is based on the zero-shear rate viscosity, and the elasticity number is thus also an upper bound.

Viscoelastic vortex growth for shear-thinning fluids in planar contractions has been documented by a number of authors [11-14, 29]. However, vortex growth has not been observed in the flow of Boger fluids through planar contractions, nor has it been numerically predicted for UCM or Oldroyd-B fluids. In fact, constant shear viscosity elastic fluids are known to show a reduction in vortex size with increasing Deborah

number in planar geometries [27]. The vortex growth that has also been predicted for PTT fluids in planar contractions shows that the strength, growth rate and size of the vortex are smaller in a planar geometry compared with the axisymmetric geometry.

3.4 Pressure drop measurements

The steady-state pressure drop measurements $\Delta P_{12}(Q)$ between two positions 6mm upstream and downstream of the contraction for a range of flowrates are presented in Figure 13(a). First note that for all flowrates (corresponding to $Re < 60$) the total pressure drop measured for water increases linearly with Q. The linear slope of the pressure drop/flowrate curve at low Q has been used to normalise differential pressure data in each fluid. Values of the initial gradient ($s = d\Delta P_{12}/dQ$ when Q ö 0) used to calculate the dimensionless pressure drop ΔP, were 4.33 kPa/(ml/hr), 1.70 and 1.63 kPa/(ml/hr) for the 0.3%, 0.1% and 0.05% PEO solutions respectively. In the limit of zero shear-rate, the ratio of these two gradients ($s^{(0.3\%\ \mathrm{PEO})} / s^{(0.1\%\ \mathrm{PEO})} = 2.55$) should equal the ratio of their zero-shear viscosities ($\eta_0^{(0.3\%\ \mathrm{PEO})} / \eta_0^{(0.1\%\ \mathrm{PEO})} = 3.58$). The discrepancy probably arises from the differing degree of shear-thinning that is experienced (primarily by the 0.3% PEO) at shear rates on the order of 10^4 s^{-1} (Figure 5). There is less discrepancy in these ratios when comparing the 0.1% PEO and 0.05% PEO solutions, since their zero-shear viscosities are closer in magnitude and they undergo approximately the same degree of shear-thinning for shear rates less than 10^4 s^{-1}. The constant dimensionless pressure drop illustrated in Figure 15(a) for water at all Re within the range tested, shows that inertial contributions to the fully-developed pressure drop in

Newtonian flows through the 16:1 contraction are negligible for $Re < 60$. However, previous work suggests that there is a strong coupling between inertia and elasticity, such that the effects of inertia on both the kinematics (ie. streaklines) and on the dynamics (ie. pressure drop) can be seen at Reynolds numbers far lower than expected [7]. This is confirmed by the streak images in Figure 10 and Figure 11, in which the interplay of inertia and elasticity evidently depends on Reynolds number.

All differential pressure measurements were performed over approximately the same range of Deborah numbers, $0 < De < 500$ for each fluid. The dimensionless pressure drop $\Delta P = \Delta P_{12}/sQ$ is shown in Figure 13. For the most elastic solution (0.3% PEO), ΔP asymptotically approaches a value of 3.5 at high *De*. This is in agreement with the pressure drop measurements of [25], who measure a limiting value of $\Delta P > 4$ in a 4:1:4 axisymmetric contraction-expansion, although for much lower values of *De* ($0 < De < 8$). The shape of the growth of ΔP over the range $0 < De < 500$, for the 0.3% PEO solution is also similar to that observed in their 0.025% wt. PIB/C14 solution in a 4:1:4 axisymmetric contraction/expansion [25].

The results for the 0.1% and 0.05% PEO solutions are more dramatic and show that a *higher* dimensionless pressure drop is observed in both cases compared with the 0.3% PEO solution. The saturation in ΔP observed for all three PEO solutions is probably a consequence of polymer chains reaching their finite extensibility limit. As polymer concentration increases, the mobility of individual polymer chains is hindered through chain-chain interactions, resulting in an overall reduction in the finite extensibility of the

polymer. Of the three solutions, only the 0.05% PEO solution has a concentration less than c^*, and consequently we find that the maximum dimensionless pressure drop decreases for increasing concentration. Of the three solutions, only the 0.05% PEO solution has a concentration less than c^*. As full extension is approached, the polymer chains act as an isotropic viscous fluid, such that $\Delta P \sim \eta_E \dot{\varepsilon} \cong Q\eta_E / (w_c^2 h)$. The local maxima in the dimensionless pressure drop for the 0.05% and 0.1% PEO solutions, compared with the plateau observed for the 0.3% PEO solution, is thought to be a result of the higher inertial effects in these lower viscosity solutions.

The maximum in the dimensionless pressure drop for the 0.05% PEO solution correlates with the bistable vortex structure, observed in Figure 11 (*El* = 3.8, *De* = 121 - 166). The pressure drop data for the 0.1% PEO solutions also contains a weak maximum; however it occurs at a *De* beyond any of those in the streak images and we are unable to provide a clear mechanism for it. Other considerations which may influence the pressure response are channel blockages (and subsequent unblocking at sufficiently high pressures), although intense fluorescence and refraction at the contraction throat limits quantitative assessment of this particle build-up.

4.0 DISCUSSION

Exploiting the high deformation rates and small lengthscales of micro-fabricated flow geometries makes it possible to generate very high shear rates and high Deborah numbers that far exceed those achievable in traditional macro-scale entry flow experiments.

Consequently, we have been able to generate strong viscoelastic effects even in dilute and semi-dilute aqueous polymer solutions. These deformation rates are representative of values that might be obtained in commercial coating and jetting operations. The importance of the geometric scale is best characterized by the elasticity number, which is independent of kinematics and only dependent on the intrinsic fluid properties (density, relaxation time, viscosity) plus a characteristic lengthscale of the device. It should however be emphasised that this kinematic independence is only true for deformations $\dot{\gamma} \ll 1/\lambda$ when the relaxation time and viscosity are constant; at higher rates, the viscometric properties shear thin and the elasticity number decreases with shear rate.

We have studied the behaviour of three dilute and semi-dilute PEO solutions in geometries with $l \approx 25\mu m$ (El = 3.8, 8.4, and 89), and characterised them in terms of the steady flow patterns observed, and the onset of inertio-elastic instabilities (at high De). Futhermore, the evolution in the dimensionless vortex length and dimensionless pressure drop with increasing flowrate has been quantified. It was found that the general characteristics of the inertio-elastic instabilities observed in the three solutions of different elasticity are grossly similar for the same value of De; however the influence of higher levels of fluid inertia reduces the temporal stability and coherence of these patterns. This is most clearly illustrated by the streak images at El = 89 in Figure 10 and Figure 11, in which coherent lip vortex and elastic corner vortex structures are readily supported. In the case of smaller elasticity numbers, the inertio-elastic instability also develops in the contraction throat, however stable lip vortex structures are not obtained.

At the highest flow rates, the stable elastic vortex growth is also associated with the formation of diverging streamlines upstream of the contraction plane, which is a feature of macro-scale circular entry flows with shear-thinning fluids [8-10, 29] and less commonly with Boger fluids [7, 35]. The precise dynamical mechanism that leads to the development of diverging streamlines upstream of the contraction plane is still unclear. The few numerical simulations that have predicted diverging flow upstream of the contraction have not focussed on this phenomenon in any detail. However it appears to require the combination of significant fluid elasticity ($De > 1$), rate-dependent material functions (such as those predicted by the PTT constitutive model) and also the effects of fluid inertia ($Re \neq 0$). In this regard it is analogous to the combination of physical properties required to generate a 'negative wake' behind a sedimenting sphere [61].

The degree of shear-thinning that occurs at the deformation rates in our experiments is not known quantitatively, however from the steady shear rheology we would expect that the highest degree of shear thinning would occur in the semi-dilute 0.3% PEO solution ($c/c^* = 3.5$). It is anticipated that the rate dependence of the material functions for the 0.1% PEO and 0.05% PEO solutions is almost negligible. The dimensionless vortex lengths measured for each of the solutions over the range $50 < De < 550$ grow in an approximately linear manner with De, and follow the expected behaviour of a fluid with a constant relaxation time [25]. The onset of appreciable vortex growth ($De \geq 50$) is preceded by the onset of a locally unsteady three-dimensional flow immediately upstream of the contraction plane.

The dimensionless pressure drop for the 0.3% PEO solution (*El* = 89) reached an asymptotic value of around 3.5 at high shear rates, which is comparable to the value measured for dilute PS/PS Boger fluids in axisymmetric contraction flow [25]. As the elasticity number is reduced (i.e. increasing the relative magnitude of inertial to elastic effects) a maximum in the dimensionless pressure drop, ΔP develops and occurs at $Re > 30$ for both 0.05% and 0.1% PEO solutions. If instead, we plot the dimensionless pressure drop, ΔP as a function of *De*, we see the growth of a local maximum in ΔP as *El* is reduced. This maximum becomes more pronounced and shifts to lower *De* as the effects of inertia increase. This "inertial" maximum observed in the dimensionless pressure drop measurements for the 0.05% and 0.1% PEO has also been observed by James and Saringer [20], in their exponentially-converging channel experiments using dilute PEO solutions. This behaviour was observed most distinctively for their *highest* concentrations, which were only $0.07c^*$ and $0.13c^*$; significantly lower than the values $0.7c^*$ and $1.34c^*$ for our 0.05% and 0.1% PEO solutions, respectively.

There is no previous work that we are aware of which presents pressure drop measurements for shear-thinning polymeric fluids flowing through planar contractions. Numerical models are currently unable to correctly predict the pressure drop in planar geometries [30] even for shear-thinning fluids, and tend to predict negative Couette correction coefficients. For constant viscosity Boger fluids, Nigen and Walters [15] measured the pressure drop in planar contractions and found that there was no difference in the pressure drop for a Boger fluid and Newtonian fluid of the same zero-shear viscosity.

This study represents one of the first detailed studies of non-Newtonian flow in microfluidic geomtries. As such, additional factors should be kept in mind. Firstly, the three-dimensional nature of the flow and the finite depth of the microscopic video imaging system makes it difficult to precisely determine instantaneous 3-dimensional streamlines, because we in fact image particle trajectories or 'streaklines'. The finite depth of the imaging system (δz_m = 27 μm) results in analysis of the streamlines over a substantial depth of the channel, rather than within a single plane. Quantitative 2D imaging (ie. by minimizing δz_m) is achievable using micro-particle image velocimetry techniques [62], and will be the subject of future experiments. The three-dimensional flow structure and time-dependent nature of the flow also contributes to the multiple streaklines assembled in each image. All of the images for $De \geq 60$ show overlapping particle pathlines. It should be kept in mind that the images associated with the 0.3% PEO solution are taken with the same exposure time (16 ms) as the other solutions. Because the flow velocities are substantially smaller, the coherence of the streak lines for the 0.3% PEO solution may therefore be deceiving as they represent a smaller path length $\delta l = |v(x)|\delta t$ than in the faster moving flows. Similar difficulties are observed in time-dependent studies of flow of Newtonian and non-Newtonian fluids in Hele-Shaw geometries [63]. It is worth noting that the very shallow depths (typically 50μm or less) of the present microfabricated channels are a characteristic of *all* microfluidic devices. Our ability to image well-defined recirculating flow structures in both Newtonian and viscoelastic steady flows near the centre-plane (Figure 8-Figure **11**) suggests that a Hele-Shaw type approach to analysis of microfluidic flows may be helpful in future computations of these three dimensional microfluidic flow geometries.

A second imaging artefact is associated with the time resolution of the image capture system relative to the frequency of vortex size oscillations. Analysis of both single frame streak images and video microscopy images led to the conclusion that the oscillation frequency of the vortex size is dependent on the flowrate. At low flowrates, instabilities can be resolved because of the slower frequency and better time resolution of the local fluctuations. At higher flowrates, the high frequency of oscillations results in an image that effectively contains an ensemble of large number of individual oscillations. Although the image will be *less defined*, as is observed for the 0.1% PEO solution at high flowrates, the flow feature (eg. vortex size) will be less variable between images. On the other hand, the vortex in the 0.3% PEO solution appears to be more clearly defined, although its size is more variable between images.

In addition to imaging artefacts, the integrity of the channel geometry as well as material build-up in the device also grossly affect the pressure drop measurements and the asymmetry of the flow. The asymmetry associated with the 0.1% and 0.3% PEO is believed to be associated with small amounts of material that has been carried by the flow, and sticks to the surface of the channel near the contraction throat. Depending on the amount of deposited material, this can effectively cause asymmetries in the geometry, resulting in asymmetric flow.

The pressure-driven flow of dilute aqueous PEO solutions, particularly at moderate Reynolds number, has been known to cause a build-up of material at the contraction

entrance [20], resulting in a build-up of "crystallised" PEO strands that would occur on timescales of the order of minutes to hours. However, the extent of this PEO buildup in the present experiments has not been determined. The streak images do show that the contraction region is particularly susceptible to a build-up of fluorescent particles. The magnitude of this particle accumulation and its effect on the flow field has not been established. Similar particle agglomerations have been observed upstream and downstream of the contraction, and detailed microscopic imaging of the fluid streamlines close to the wall (not reproduced here) suggest that they do not impose any disturbance on the flow.

Larger masses of particle build-up and the presence of material in the solution (believed to be a by-product of the channel fabrication process), can however lead to partial channel blockages (and subsequent unblocking at sufficiently high pressures), which are likely to influence the pressure response. These are difficult to control, however they can be monitored by microscopic observation during pressure measurements. Intense fluorescence and refraction at the contraction throat limits quantitative assessment of smaller agglomerations.

Returning to the *De-Re* parameter space that was introduced in section 1, the evolution in the dynamical behaviour of the three polymer solutions at El = 3.8, 8.4 and 89 is characterised by the development of a number of specific flow regimes. In Figure 15 we illustrate these flow regimes, and their location in *De-Re* space. For all three solutions, the onset of elastic instabilities close to the throat is manifested by the development of

additional curvature and fluctuations in the streamlines at a critical $De_{crit} > 50$. In the case of high levels of fluid elasticity ($El = 89$), this is followed by the development of coherent and stable lip vortices for $50 < De < 100$, which subsequently develop into asymmetric viscoelastic corner vortices that continue to grow upstream for $De > 100$. For lower levels of fluid elasticity, inertio-elastic instabilities upstream of the contraction plane at $De_{crit} > 50$, replace the lip vortices observed at higher elasticity numbers. For $100 < De < 150$, elastic vortices grow steadily upstream. These vortices are essentially symmetric for $El = 9$ but are temporally-unsteady and spatially-bistable structures for $El = 3.8$. Diverging streamlines eventually develop for $De > 150$, just upstream of the elastic vortex structures. These appear to be a common feature to flows that are governed by the competing effects of inertia and fluid elasticity [8, 9].

5.0 CONCLUSIONS

The behaviour of low viscosity, elastic solutions of PEO in water within 16:1 micro-fabricated contractions have been characterised in terms of the steady flow patterns observed, the onset of inertio-elastic instabilities plus the evolution in the dimensionless vortex length and dimensionless pressure drop with increasing flowrate. The high deformation rates and small lengthscales afforded by micro-fabricated flow geometries make it possible to generate very high shear rates and high Deborah numbers that far exceed those achievable in traditional macro-scale entry flow experiments, generating strong viscoelastic effects even in dilute and semi-dilute aqueous polymer solutions. The present experiments confirm the importance of the geometric scale, which is characterised by the elasticity number; a dimensionless quantity that is independent of kinematics and only dependent on the intrinsic fluid properties (density, relaxation time, viscosity) plus a characteristic lengthscale of the device.

It was found that the general characteristics of the inertio-elastic instabilities observed in the three solutions of different *El* (varying from 3.8 to 89) is approximately the same for the same Deborah number; however, the influence of higher levels of fluid inertia reduces the temporal stability and coherence of these patterns. A number of flow regimes corresponding to the development of inertio-elastic instabilities, vortex growth and diverging flow have been elucidated according to their position in *De-Re* space. This clearly illustrates the effect of the elasticity number, and the effect of the relative

magnitudes of inertial and elastic contributions to fluid motion on the evolution of inertio-elastic flow structures.

The present work has important implications in the design and operation of micron-scale processes that involve the transportation of dilute aqueous polymer solutions, such as lab-on-a-chip and inkjet devices. Furthermore, the expansive region of *De-Re* space that is accessible in microfluidic geometries is unparalleled by macro-scale experimental geometries, and provides a simple means of probing a wide range of elasticity numbers. The present experiments are useful in testing the performance of current constitutive models over a wide range of flow conditions; and also of use in testing the performance of current unsteady and/or three-dimensional numerical codes that incorporate elasticity, inertia and constitutive non-linearities.

ACKNOWLEDGMENTS

The authors would like to thank the Smorgon family for their financial support through the Eric and Anne Smorgon Memorial Award, the Particulate Fluids Processing Centre at the University of Melbourne for infrastructure and support, the Schlumberger Foundation, and the Institute for Soldier Nanotechnology (ISN) at MIT.

6.0 NOMENCLATURE

Dimensionless Groups

Re, Re_{crit}	Reynolds number, and critical value	-
$\tilde{Re}$	Modified Reynolds number	-
De, De_{crit}	Deborah number, and critical value	-
Wi, Wi_{crit}	Weissenberg number, and critical value	-
El	Elasticity number	-
Ta, Ta_{crit}	Taylor number, and critical value	-

Geometric Properties

L	Characteristic lengthscale	m
H	Channel depth	m
D	Diameter of tube	m
w_u, w_c	Upstream channel and contraction widths	m
L_c	Contraction length	m
L_v	Vortex length	m
χ_L	Dimensionless vortex length	-
β	Contraction ratio	-
α	Wall angle	-
$\varepsilon = d/R_1$	Ratio of gap to inner cylinder radius in Couette cell geometry	-
F_θ	Geometric factor for shear stress (conversion factor in	-

	rheometer)	
z	Axial distance downstream of contraction plane	m

Dynamic Properties

Q	Volumetric flowrate	$m^3.s^{-1}$
$\dot{\gamma}$	Shear rate	s^{-1}
$\dot{\gamma}_{crit}$	Critical shear rate	s^{-1}
$\bar{V}, V$	Average or characteristic velocity	$m.s^{-1}$
τ_{flow}	Characteristic timescale of the flow	
$\bar{V}_c$	Average velocity in the contraction	$m.s^{-1}$
$\bar{V}_u$	Average velocity upstream of the contraction	$m.s^{-1}$
Ω_1	Angular rotation of inside cylinder of Couette cell	s^{-1}
ω	Angular frequency associated with oscillatory shear tests	s^{-1}
$v(x)$	Point velocity	$m.s^{-1}$
δt	Arbitrary time step	s
$\Im_{min}$	Minimum torque	N.m
ΔP, ΔP_{max}	Dimensionless pressure drop, and maximum value	-
ΔP_{12}	Pressure drop across contraction	kPa
ΔP_{en}	Entrance pressure drop	kPa
s	Gradient of $\Delta P_{12} - Q$ curve at low flowrates	$kPa/(m^3.s^{-1})$

Rheological Properties

$\eta_s, \eta_p,$	Solvent and polymer viscosity	Pa.s
η, η_E	Shear and extensional viscosity	Pa.s
N_1	First normal stress difference	Pa
Ψ_1	First normal stress coefficient	$Pa.s^2$
τ	Shear stress	Pa.s
S	Stress ratio	-
G'	Storage modulus	Pa
η'	Dynamic viscosity	Pa.s
λ_{Zimm}	Zimm relaxation time	s
λ	CaBER-determined relaxation time	s
$[\eta]$	Intrinsic viscosity	$ml.g^{-1}$
ρ	Fluid density	$kg.m^{-3}$
c, c^*	Concentration, overlap concentration	%wt, ppm
M_W	Molecular weight	$g.mol^{-1}$
ϕ	Volume fraction	-
N	No. of Kuhn steps	-
B	Size of a Kuhn step	m
R_{max}	Maximum length of a polymer chain (at full stretch)	m

Constitutive Parameters

n	Power law exponent	-
K	Power law coefficient	$Pa.s^{(n-1)}$
ε	Finite extensibility parameter in PTT model	-
v	Solvent quality ($v = (a' + 1)/3$)	-
a'	Exponent in Mark-Houwink relation	-

Optical Parameters

NA	Numerical aperture	-
n	Refractive index	-
λ_0	Wavelength of light in a vacuum	m
δz_m	Measurement depth	m
δz (or DOF)	Depth of field	m
θ	Aperture angle of objective lens	-
d_p	Particle diameter	m
e	Minimum resolvable distance by detector on image plane	m
M	Magnification	-

Physical Constants

N_A	Avogadro's constant	-
k_B	Boltzmann constant	$J.K^{-1}$

Abbreviations

A	Axisymmetric
P	Planar
S	Square
LDV	Laser Doppler Anemometry
FIB	Flow induced Birefringence
FEM	Finite Element Model
FVM	Finite Volume Model
UCM	Upper Convected Maxwell
PTT	Phan-Thien Tanner

7.0 REFERENCES

1. Mitchell, P., *Microfluidics - downsizing large-scale biology.* Nature Biotechnology, 2001. **19**(8): p. 717-721.
2. Groisman, A., M. Enzelberger, and S. Quake, *Microfluidic memory and control devices.* Science, 2003. **300**: p. 955-958.
3. Groisman, A. and S. Quake, *A microfluidic rectifier: anisotropic flow resistance at low Reynolds numbers.* Physical Review Letters, 2004. **92**(9): p. 094501-1 - 094501-4.
4. Choi, C.-H., K.J.A. Westin, and K.S. Breuer, *Slip Flows in Hydrophilic and Hydrophobic Microchannels.* Physics of Fluids, 2003. **15**(10): p. 2897-2902.
5. Zhu, T. and S. Granick, *Limits of the Hydrodynamic No-Slip Boundary Condition.* Physical Review Letters, 2002. **88**: p. 106102.
6. Dontula, P., C.W. Macosko, and L.E. Scriven, *Model elastic liquids with water-soluble polymers.* AIChE Journal, 1998. **44**(6): p. 1247-1255.
7. Boger, D.V. and R.J. Binnington, *Circular Entry Flows of Fluid M1.* Journal of Non-Newtonian Fluid Mechanics, 1990. **35**(2-3): p. 339-360.
8. Cable, P.J. and D.V. Boger, *A comprehensive experiental investigation of tubular entry flow of viscoelastic fluids; Part II. The velocity field in stable flow.* AIChE Journal, 1978. **24**(6): p. 992-999.
9. Cable, P.J. and D.V. Boger, *A comprehensive experiental investigation of tubular entry flow of viscoelastic fluids; Part III. Unstable Flow.* AIChE Journal, 1979. **25**(1): p. 152-159.
10. Cable, P.J. and D.V. Boger, *A comprehensive experiental investigation of tubular entry flow of viscoelastic fluids; Part I. Vortex characteristics in stable flow.* AIChE Journal, 1978. **24**(5): p. 869-879.
11. Evans, R.E. and K. Walters, *Further remarks on the lip-vortex mechanism of vortex enhancement in planar-contraction flows.* Journal of Non-Newtonian Fluid Mechanics, 1989. **32**: p. 95-105.
12. Evans, R.E. and K. Walters, *Flow characteristics associated with abrupt changes in geometry in the case of highly elastic liquids.* Journal of Non-Newtonian Fluid Mechanics, 1986. **20**: p. 11-29.
13. Chiba, K., T. Sakatani, and K. Nakamura, *Anomalous flow patterns in viscoelastic entry flow through a planar contraction.* Journal of Non-Newtonian Fluid Mechanics, 1990. **36**: p. 193-203.
14. Chiba, K., S. Tanaka, and K. Nakamura, *The structure of anmoalous entry flow patterns through a planar contraction.* Journal of Non-Newtonian Fluid Mechanics, 1992. **42**: p. 323-350.
15. Nigen, S. and K. Walters, *Viscoelastic contractions flows: comparison of axisymmetric and planar configurations.* Journal of Non-Newtonian Fluid Mechanics, 2002. **102**: p. 343-359.
16. Boger, D.V., *Viscoelastic Flows Through Contractions.* Annual Review of Fluid Mechanics, 1987. **19**: p. 157-182.
17. White, S.A., A.D. Gotsis, and D.G. Baird, *Review of the entry flow problem: Experimental and numerical.* Journal of Non-Newtonian Fluid Mechanics, 1987. **24**: p. 121-160.

18. Raiford, W.P., et al., *LDV Measurements of Viscoelastic Flow Transitions in Abrupt Axisymmetric Contractions - Interaction of Inertia and Elasticity.* Journal of Non-Newtonian Fluid Mechanics, 1989. **32**(1): p. 39-68.
19. Boger, D.V., M.J. Crochet, and R.A. Keiller, *On viscoelastic flows through abrupt contractions.* Journal of Non-Newtonian Fluid Mechanics, 1992. **44**: p. 267-279.
20. James, D.F. and J.H. Saringer, *Flow of dilute polymer solutions through converging channels.* Journal of Non-Newtonian Fluid Mechanics, 1982. **11**: p. 317-339.
21. Quinzani, L.M., R.C. Armstrong, and R.A. Brown, *Use of coupled birefringence and LDV studies of flow through a planar contraction to test constitutive equations for concentrated polymer solutions.* Journal of Rheology, 1995. **39**(6): p. 1201-1228.
22. Walters, K. and D.M. Rawlinson, *On some contraction flows for Boger fluids.* Rheologica Acta, 1982. **21**: p. 547-552.
23. Boger, D.V., D.U. Hur, and R.J. Binnington, *Further Observations of Elastic Effects in Tubular Entry Flows.* Journal of Non-Newtonian Fluid Mechanics, 1986. **20**: p. 31-49.
24. Nguyen, H. and D.V. Boger, *Kinematics and Stability of Die Entry Flows.* Journal of Non-Newtonian Fluid Mechanics, 1979. **5**(APR): p. 353-368.
25. Rothstein, J.P. and G.H. McKinley, *The axisymmetric contraction-expansion: the role of extensional rheology on vortex growth dynamics and the enhanced pressure drop.* Journal of Non-Newtonian Fluid Mechanics, 2001. **98**(1): p. 33-63.
26. Chiba, K. and K. Nakamura, *Instabilities in a circular entry flow of dilute polymer solutions.* Journal of Non-Newtonian Fluid Mechanics, 1997. **73**(1-2): p. 67-80.
27. Alves, M.A., P.J. Oliveira, and F.T. Pinho. *Numerical simulation of viscoelastic contraction flows*. in *Second MIT Conference on Computational Fluid and Solid Mechanics*. 2003. MIT: Elsevier Science Ltd.
28. Purnode, B. and M.J. Crochet, *Flows of polymer solutions through contractions. Part 1: flows of polyacrylamide solutions through planar contractions.* Journal of Non-Newtonian Fluid Mechanics, 1996. **65**: p. 269-289.
29. Alves, M.A., *Escoamentos de fluidos viscoelásticos em regime laminar*, in *Faculty of Engineering*. 2004, University of Porto: Porto, Portugal.
30. Alves, M.A., P.J. Oliveira, and F.T. Pinho, *Benchmark solutions for the flow of Oldroyd-B and PTT fluids in planar contractions.* Journal of Non-Newtonian Fluid Mechanics, 2003. **110**: p. 45-75.
31. Alves, M.A., F.T. Pinho, and P.J. Oliveira, *Effect of a high-resolution differencing scheme on finite-volume predictions of viscoelastic flows.* Journal of Non-Newtonian Fluid Mechanics, 2000. **93**(2-3): p. 287-314.
32. Alves, M.A., et al. *Visualization studies of viscoelastic flow in a 4:1 square/square contraction*. in *17th International Congress of Mechanical Engineering*. 2003. São Paulo, SP.
33. Phillips, T.N. and A.J. Williams, *Comparison of creeping and inertial flow of an Oldroyd B fluid through planar and axisymmetric contractions.* Journal of Non-Newtonian Fluid Mechanics, 2002. **108**(1-3): p. 25-47.
34. Oliveira, P.J. and F.T. Pinho, *Plane contraction flows of upper convected Maxwell and Phan-Thien-Tanner fluids as predicted by a finite-volume method.* Journal of Non-Newtonian Fluid Mechanics, 1999. **88**: p. 63-88.
35. Mckinley, G.H., et al., *Nonlinear Dynamics of Viscoelastic Flow in Axisymmetrical Abrupt Contractions.* Journal of Fluid Mechanics, 1991. **223**: p. 411-456.
36. Xue, S.-C., N. Phan-Thien, and R.I. Tanner, *Three dimensional numerical simulations of viscoelastic flows through planar contractions.* Journal of Non-Newtonian Fluid Mechanics, 1998. **74**: p. 195-245.

37. Baloch, A., P. Townsend, and M.F. Webster, *On vortex development in viscoelastic expansion and contraction flows.* Journal of Non-Newtonian Fluid Mechanics, 1996. **65**(2-3): p. 133-149.
38. McDonald, J.C., et al., *Fabrication of microfluidic systems in poly(dimethylsiloxane).* Electrophoresis, 2000. **21**(1): p. 27-40.
39. Ng, J.M.K., et al., *Components for integrated poly(dimethylsiloxane) microfluidic systems.* Electrophoresis, 2002. **23**: p. 3461-3473.
40. Scott, T.P., *Contraction/Expansion Flow of Dilute Elastic Solutions in Microchannels*, in *Department of Mechanical Engineering*. 2004, MIT: Cambridge.
41. Rodd, L.E., et al., *Capillary Break-up Rheometry of Low-Viscosity Elastic Fluids.* Applied Rheology, 2004 (submitted).
42. Tirtaatmadja, V., G.H. McKinley, and J.J. Cooper-White, *Drop formation and breakup of low viscosity elastic fluids: effects of molecular weight and concentration.* Physics of Fluids, 2004: p. (submitted).
43. Graessley, W.W., *Polymer chain dimensions and the dependence of viscoelastic properties on concentration, molecular weight and solvent power.* Polymer, 1980. **21**: p. 258-262.
44. Bazilevskii, A.V., V.M. Entov, and A.N. Rozhkov, *Failure of Oldroyd liquid bridge as a method for testing the rheological properties of polymer solutions.* Polymer Science Ser. A (translated from Vysokomolekulyarnye Soedineniya, Ser. A pp 474-482), 2001. **43**(7): p. 1161-1172.
45. Stelter, M., et al., *Investigation of the elongational behavior of polymer solutions by means of an elongational rheometer.* Journal of Rheology, 2002. **46**(2): p. 507-527.
46. Tam, K.C. and C. Tiu, *Steady and Dynamic Shear Properties of Aqueous polymer Solutions.* Journal of Rheology, 1989. **33**(2): p. 257-280.
47. Larson, R., *Instabilities in viscoelastic flows.* Rheologica Acta, 1992. **31**: p. 213-263.
48. Macosko, C.W., *Rheology Principles, Measurements and Applications*. 1994, New York: Wiley-VCH. 181-235.
49. Meinhart, C.D., S.T. Wereley, and M.H.B. Gray, *Volume illumination for two-dimensional particle image velocimetry.* Measurement Science and Technology, 2000. **11**: p. 809-814.
50. Dealy, J.M., *On the significance of pressure relaxations in capillary or slit flow.* Rheologica Acta, 1995. **34**: p. 115-116.
51. Barnes, H.A., J.F. Hutton, and K. Walters, *An Introduction to Rheology*. 1989, Amsterdam: Elsevier Science Pub. Co.
52. Stokes, J.R., et al., *Swirling flow of viscoelastic fluids. Part 1. Interaction between inertia and elasticity.* Journal of Fluid Mechanics, 2001. **429**: p. 67-115.
53. Rothstein, J.P. and G.H. McKinley, *Extensional flow of a polystyrene Boger fluid through a 4: 1: 4 axisymmetric contraction/expansion.* Journal of Non-Newtonian Fluid Mechanics, 1999. **86**(1-2): p. 61-88.
54. Boger, D.V. and K. Walters, *Rheological Phenomena in Focus*. Rheology Series, 4. 1993, New York: Elsevier.
55. Townsend, P. and K. Walters, *Expansion flows of non-Newtonian liquids.* Chemical Engineering Science, 1994. **49**(5): p. 749-763.
56. Mishra, S. and K. Jayaraman, *Asymmetric flows in planar symmetric channels with large expansion ratio.* International Journal for Numerical Methods in Fluids, 2002. **38**(10): p. 945-962.
57. Fearn, R.M., T. Mullin, and K.A. Cliffe, *Nonlinear flow phenomena in a symmetric sudden expansion.* Journal of Fluid Mechanics, 1990. **211**: p. 595-608.
58. Drikakis, D., *Bifurcation phenomena in incompressible sudden expansion flows.* Physics of Fluids, 1997. **9**(1): p. 76-87.

59. Hawa, T. and Z. Rusak, *The dynamics of a laminar flow in a symmetric channel with a sudden expansion.* Journal of Fluid Mechanics, 2001. **436**: p. 283-320.
60. Alves, M.A., P.J. Oliveira, and F.T. Pinho, *On the Effect of Contraction Ratio in Viscoelastic Flow Through Abrupt Contractions.* Journal of Non-Newtonian Fluid Mechanics, 2004 (in press).
61. McKinley, G.H., *Steady and Transient Motion of Spherical Particles in Viscoelastic Liquids*, in *Transport Processes in Bubbles, Drops and Particles*, R.P. Chhabra and D. De Kee, Editors. 2002, Taylor & Francis: New York.
62. Devasenathipathy, S., et al., *Particle imaging techniques for microfabricated fluidic systems.* Experiments in Fluids, 2003. **34**: p. 504-514.
63. Maw, W.S., et al., *Effect of elasticity of a polymer solution on the Hele-Shaw flow.* Journal of Visualization, 2004. **7**(2): p. 119-126.

LIST OF FIGURES

Figure 1. Representing contraction flow experiments on a *De-Re* diagram; using (a) shear-thinning viscoelastic fluids such as concentrated polymer solutions and (b) Boger fluids consisting of dilute polymer solutions in a viscous solvent. The inclination of the lines gives the elasticity number $El = De/Re = \lambda\eta/\rho l^2$.

Figure 2. Accessing new regions of *De-Re* space through microfluidics; comparison of previous "macro-scale" entry flow experiments with the current experiments in micro-fabricated planar geometries (shown by hollow black symbols: (◊) 0.3% PEO, (□) 0.1% PEO and (o) 0.05% PEO.

Figure 3. Planar micro-fabricated contraction; w_c is the contraction width, w_u is the upstream width, L_v is the vortex length and h is the uniform depth of the channel

Figure 4. SEM images of the 16 to 1 planar contraction; (a) a "polymer's eye-view" as it enters the entrance region (b) plan view of the contraction-expansion geometry and (c) optical micrograph of the micro-channel cross-section illustrating the high wall angles ($87^o < a < 92^o$) upstream stream of the contraction plane.

Figure 5. Steady shear data for 0.1% and 0.3% PEO solutions and de-ionized water; -- minimum torque, – – onset of Taylor instabilities

Figure 6. Flow visualisation set-up; fluorescence imaging of 1.1 micron particles using a 10X 0.3NA objective and long exposure to generate streak images.

Figure 7a. Calibration points for three differential pressure sensors, able to measure maximum differential pressures of ΔP_{12} = 34.5kPa, 103kPa, and 207kPa. These are denoted by 5psi, 15psi, and 30psi, respectively.

Figure 7b. Pressure increase with time for increasing flow rates (0 ml/hr - 6 ml/hr). Flowrates are increased 1 ml/hr every 5 minutes. Data is taken using a Newtonian 55% glycerol and water mixture (η_0 = 8.59 mPa s) in a 400:25 μm contraction. Time lag is on the on the order of 5 minutes at the lowest flow rates, but decreases as flow rate increases.

Figure 8. Comparison of Newtonian and non-Newtonian entrance planar entry flows at the same *Re*; (a) 0.05% PEO and (b) DI water in a 16:1 contraction-expansion for $4 \leq Re \leq 60$.

Figure 9. The development of streaklines in the flow of 0.05% PEO in the 16:1 planar contraction in the bending streamlines – vortex growth transition regime. This

transition occurs over the range of flowrates corresponding to $18 \leq Re \leq 24$ and $68 \leq De \leq 91$.

Figure 10. Effect of the elasticity number; Streak images of 0.05% PEO (*El* = 3.8), 0.1% PEO (*El* = 8.4) and 0.3% PEO (*El* = 89) flowing through a 16:1 planar contraction around the onset of non-Newtonian behaviour, for the same De, 40 d De d 80.

Figure 11. Effect of the elasticity number; Streak images of 0.05% PEO (*El* = 3.8), 0.1% PEO (*El* = 8.4) and 0.3% PEO (*El* = 89) flowing through a 16:1 planar contraction during vortex growth, for the same *De*, 215 d *De* d 280.

Figure 12. Dimensionless vortex length as a function of *De*; (▲) 0.05% PEO (*El* = 3.8), (■) 0.1% PEO (*El* = 8.4) and (•) 0.3% PEO (*El* = 89).

Figure 13. Total Pressure drop (ΔP_{12}) versus flowrate (Q) for the (Δ) 0.05% PEO, (■) 0.1% PEO, (•) 0.3% PEO polymer solutions and for (▲) water flowing through a 16:1 planar contraction; (a) all data and (b) determining slope at low flowrates for normalizing pressure data

Figure 14. Dimensionless pressure drop versus (a) *Re* and (b) *De* for (Δ) 0.05% PEO, (■) 0.1% PEO, (•) 0.3% PEO and (▲) water ((a) only) in a 16 :1 planar contraction

Figure 15. Summary of flow regimes in *De-Re* space for semi-dilute aqueous PEO solutions through micro-fabricated geometries

TABLES

Table 1 Literature Review

Table 2 Rheological properties of solutions containing 2×10^6 MW PEO

Fluid Property (at 20°C)	0.05% PEO	0.1% PEO in water	0.3% PEO in water
Relaxation time, λ (ms)	0.7 (adjusted CaBER) 0.341 (Zimm) – 1.2 (CaBER)	1.5	4.4
Zero-shear viscosity, η_0 (mPa.s)	1.8	2.3	8.3
Density, ρ (g/cm^3)	0.996	0.996	0.989
c/c^*	0.58	1.17	3.50
c^* (wt. %)	0.0858	0.0858	0.0858

Table 1: Summary of previous entry flow studies; axisymmetric and planar geomtries

Author	Year	Keywords	Exp./Num.	Planar/Axi.	Contraction Ratio	Fluid	Rheology	De range	Re range	Comments
Alves et al.	**2004 [29]**	Elastic, elastic and shear-thinning. Creeping and inertial	E	S	4	0.01-0.05% PAA in glycerol/water	Ψ_1, η,η', ρ, G', G", N_1	0<De<0.6	2.72×10^{-5}<Re<0.012	Inertial suppression of vortices and diverging flow. Vortex growth and diverging beyond critical De. Asymmetric growth and swirling flow at high De.
Nigen and Walters	**2002**	Elastic, creeping. Boger fluid, creeping flow	E	A, P	2, 4, 8, 16, 22, 32, 40	PAA in glucose syrup/water	G', G", η, ρ	No relaxation time	0<Re<0.15	Dimensionless pressure drop > 1 observed for Boger fluid in axisymmetric contraction. (Pressure normalised by pressure drop of a newtonian fluid of the same η_0, for the same flowrate). Pressure drop for Boger fluid equal to the pressure drop of a Newtonian fluid (of the same η_0,) in planar contraction.
Quinzani et al.	**1995**	Shear-thinning and elastic. Inertial	E	P	4	5% PIB	Ψ_1, η	0.25<De<0.77	0.08<Re<1.43	No visualisation, centreline velocity only. Decrease in transient extensional viscosity with increasing De.
Chiba et al.	**1990, 1992**	Shear-thinning and elastic. Inertial	E	P	3.33, 5, 10	0.1-0.5% PAA in water	η	1.44<De<16.84	0.49<Re<331.3	Rheology of Evans and Walters 1989 used for 0.1% and of Chiba 1997 for 0.5% to calculate relaxation times. Visualise unstable streamlines along depth of channel; Goertler-like vortices.
Evans and Walters	**1986, 1989**	Shear-thinning and elastic. Inertial and creeping	E	P, S (with and without contraction <90° angle)	4, 16 (planar), 80 (axisymmetric)	0.2-2%PAA in water	N_1, η	0<De<4	0.001<Re<100	Salient vortex growth observed for shear-thinning fluid. No vortex growth for Boger fluid. No lip vortices for both fluids.
James and Saringer	**1982**	Elastic, inertial	E	A (converging)	Sink flow	5-40ppm PEO in water	Not provided	0.3<De<96	10<Re<300	De calculated using Zimm time. Dimensionless pressure drop dependent on concentration, Re and De. Unstable flow patterns.
Walters and Rawlinson	**1982**	Elastic, creeping	E	P, S	13.33	Boger fluilds, B12-17	η_0, λ	0.08<De<1.81	0.01<Re<0.23	Symmetric and asymmetric vortex growth observed for square contraction only. No vortex growth observed in planar contraction.
Alves et al.	**2004 (i) (in press)**	Shear-thinning, creeping	N	P	4, 10, 20, 40, 100	Shear-thinning fluid	PTT (ε=0.25), η_s/η_0=1/9	0<De<300	Re=0	For β>10, streamlines in corner vortex collapse at same De/β. Streamlines in lip vortex collapse at same De. Lip vortex dependent on downstream lengthscales and salient vortex dependent on upstream vortices. Upstream lengthscale important for β<10.
Alves et al.	**2003 [27]**	Elastic, shear thinning and elastic. Creeping	N	P, A	4	Oldroyd-B and PTT	Oldroyd-B, PTT (ε=0.25), η_s/η_0=1/9	0<De<1000 (PTT), 2.5 (Oldroyd-B)	Re = 0	Vortex growth for Oldroyd-B fluid in axisymmetric, vortex reduction in planar. Newtonian vortex size smaller in planar than axisymmetric. Vortex growth observed in PTT fluid for both axisymmetric and planar, however to a lesser degree in planar.
Alves et al.	**2003 [30]**	Elastic, shear-thinning and elastic. Creeping	N	P	4	Constant viscosity, elastic fluid and shear-thinning fluid	Oldroyd-B, PTT (ε=0.25), η_s/η_0=1/9	0<De<3 (Oldroyd-B) 0<De<100 (PTT)	Re=0	Decreasing salient vortex size with increasing De. Model unable to predict pressure drop (predicts negative Couette correction coefficient).
Phillips and Williams	**2002**	Elastic, inertial and creeping	N	P, A	4	Oldyroyd-B, with β>0.9 for comparison with Boger fluids	Oldroyd-B model	0<De<1.5	0<Re<1	Inertial suppression of vortices observed for both axisymmetric and planar. Net vortex growth occurred in axisymmetric and vortex reduction in planar.
Alves et al.	**2000**	Elastic, creeping and inertial	N	P	4	Constant viscosity, elastic fluid	UCM	0<De<5	Re = 0.01	No vortex growth. Vortex size reduces with increase De (constant Re). Diverging flow at highest De.
Xue et al.	**1998**	Elastic, shear-thinning and elastic. Creeping and inertial.	N	P	4	Constant viscosity, elastic fluid and shear-thinning fluid	UCM, PTT	0<De<4.4	0.06<Re<0.6	Vortex growth at small Re =0.06 for increasing De. For higher Re = 0.6, no salient vortex growth but lip vortex grows for increasing De.
Purnode and Chrochet	**1996**	Shear-thinning and elastic. Creeping and inertial	N	P	4	FENE-P (to simulate dilute PAA in water)	N_1, η	0.033<De<145	3*10^-5<Re<6.37	Lip, salient vortex growth, inertial damping of vortices. Diverging flow at highest Re and De. Qualitative agreement with Evans and Walters aqueous PAA in planar contractions.
Baloch et al.	**1996**	Shear-thinning and elastic. Inertial	N	P (contraction), P and A (expansion)	4, 13.3, 40, 80	PTT fluid with ε=0.02 (dilute polymer solution), 0.25 (polymer melt)	PTT model	1<De<25	1<Re<4	Lip vortices, growing salient vortices, diverging flow dependent on Re, De and El.

FIGURES

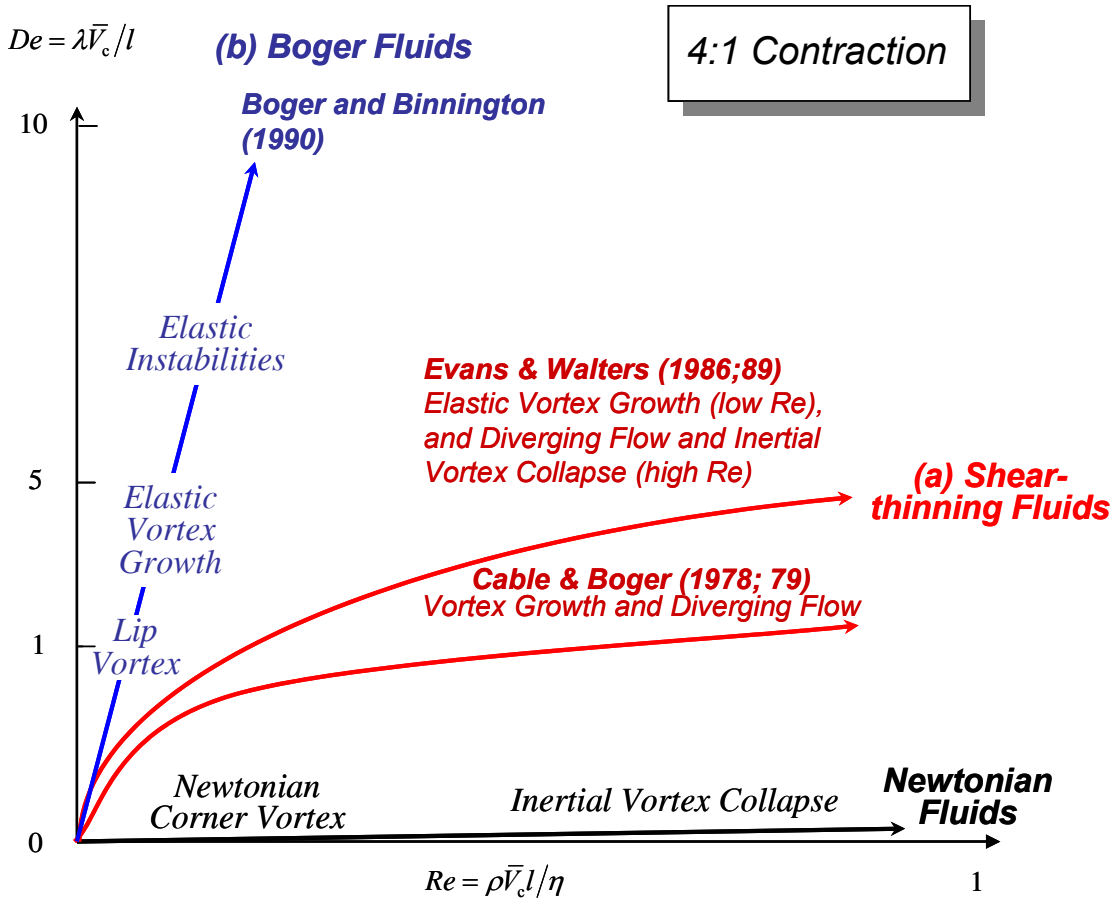

Figure 1. Representing contraction flow experiments on a *De-Re* diagram; using (a) shear-thinning viscoelastic fluids such as concentrated polymer solutions and (b) Boger fluids consisting of dilute polymer solutions in a viscous solvent. The inclination of the lines gives the elasticity number $El = De / Re = \lambda \eta / \rho l^2$.

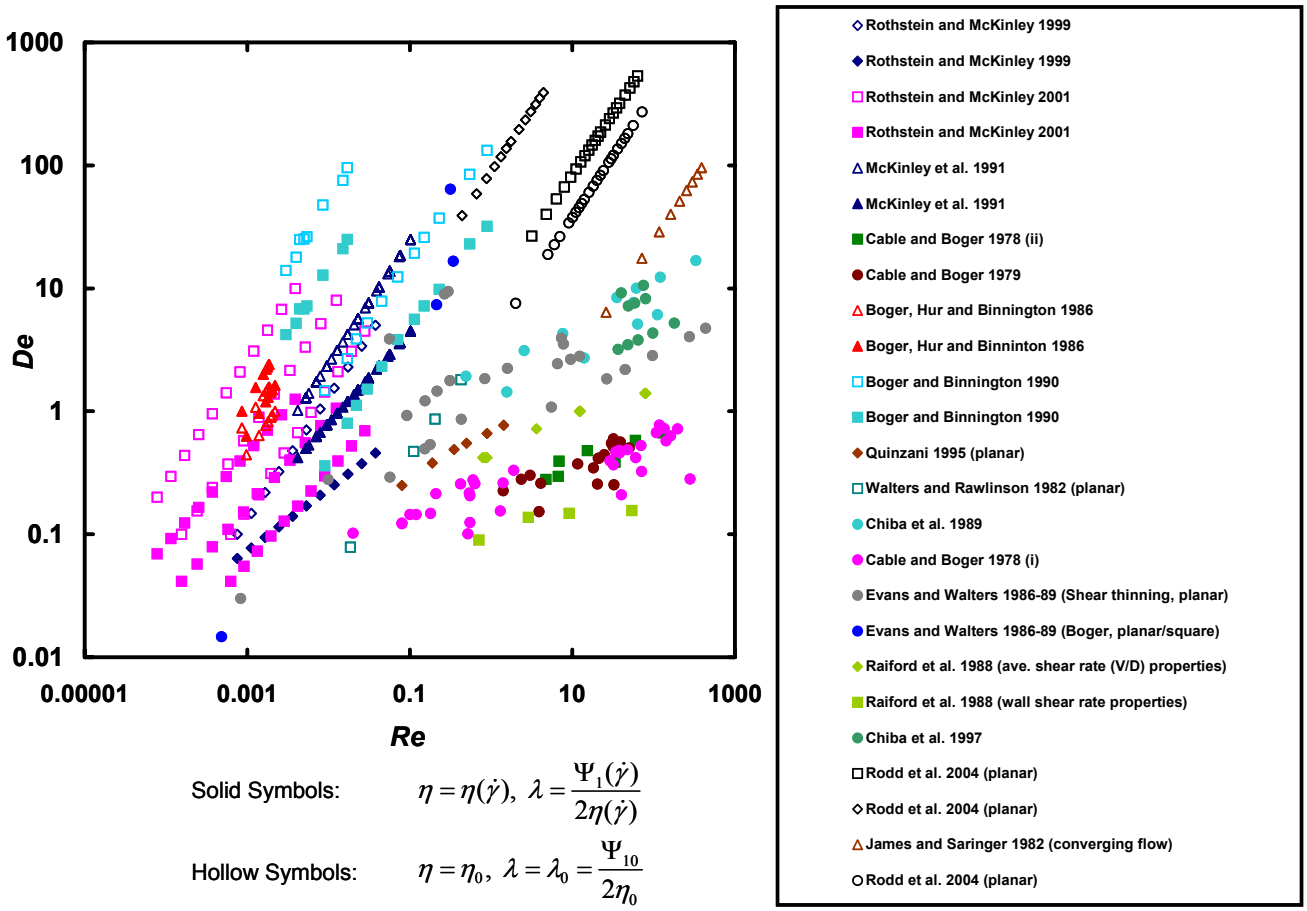

Figure 2. Accessing new regions of *De-Re* space through microfluidics; comparison of previous "macro-scale" entry flow experiments with the current experiments in micro-fabricated planar geometries (shown by hollow black symbols: (◊) 0.3% PEO, (□) 0.1% PEO and (o) 0.05% PEO.

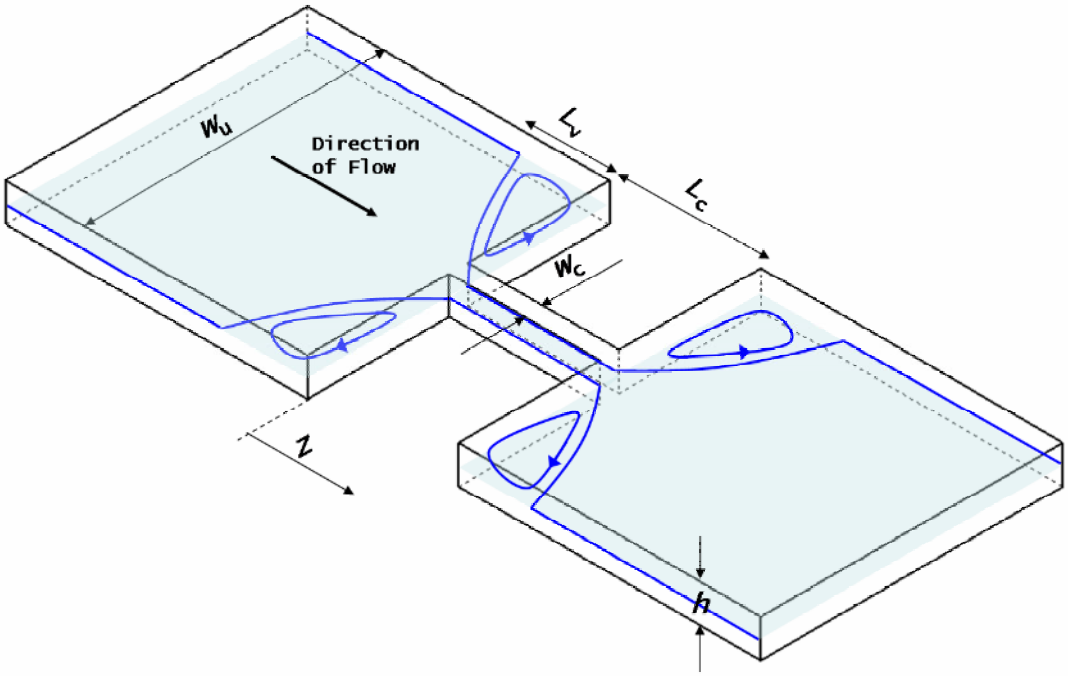

Figure 3. Schematic diagram of the planar micro-fabricated contraction-expansion; w_c is the contraction width, w_u is the upstream width, L_v is the vortex length and h is the uniform depth of the channel

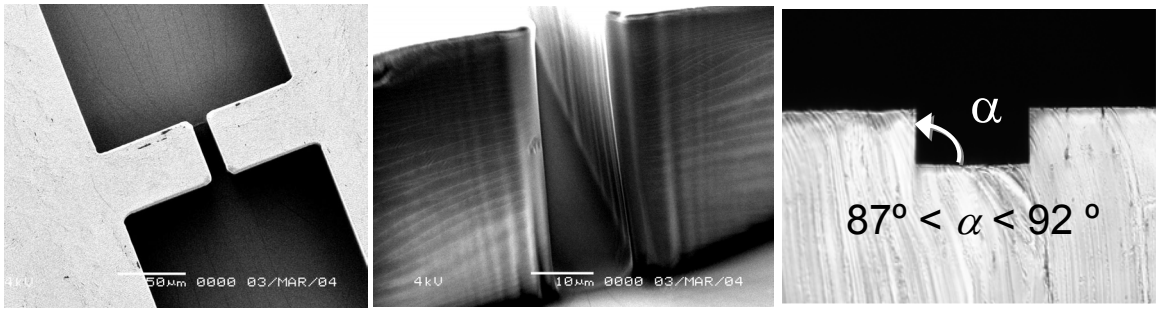

(a) (b) (c)

Figure 4. SEM images of the 16 to 1 planar contraction; (a) plan view of the contraction-expansion geometry (b) a "polymer's eye-view" as it enters the entrance region, and (c) optical micrograph of the micro-channel cross-section upstream of the contraction plane illustrating the orthogonality of the channel walls and floor ($87^o < \alpha < 92^o$).

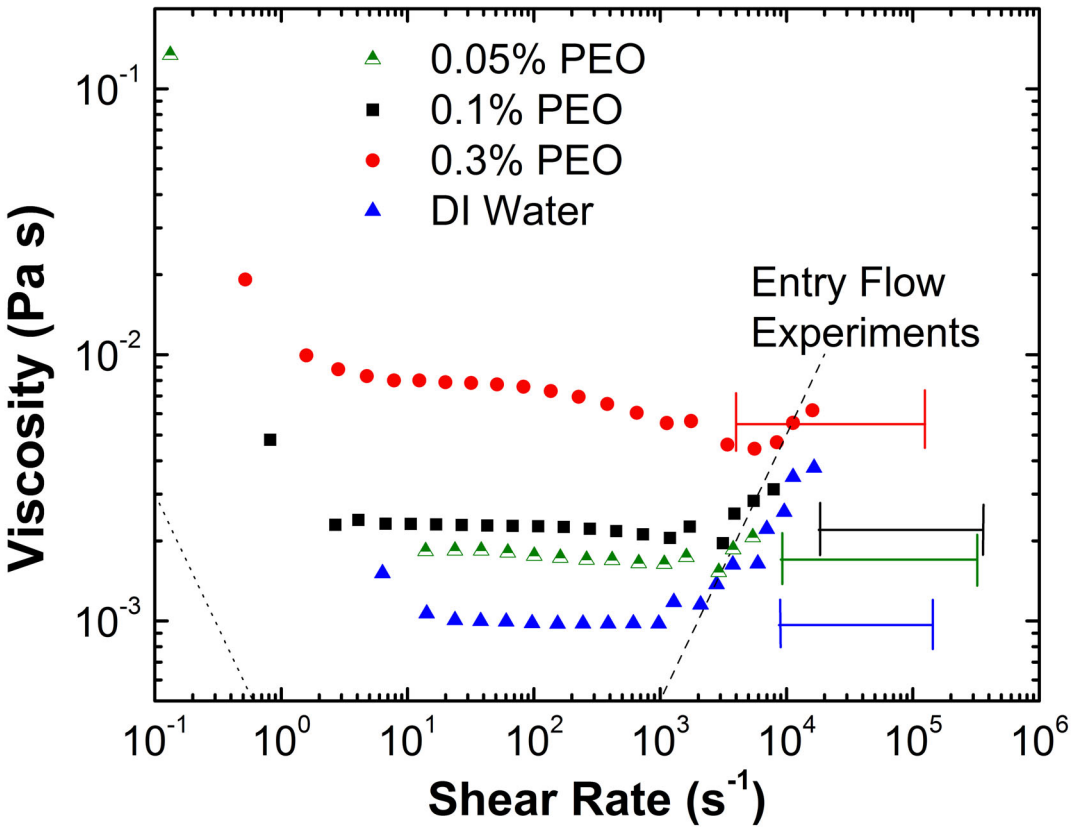

Figure 5. Steady shear data for 0.1% and 0.3% PEO solutions and de-ionized water; --- minimum torque, – – onset of Taylor instabilities.

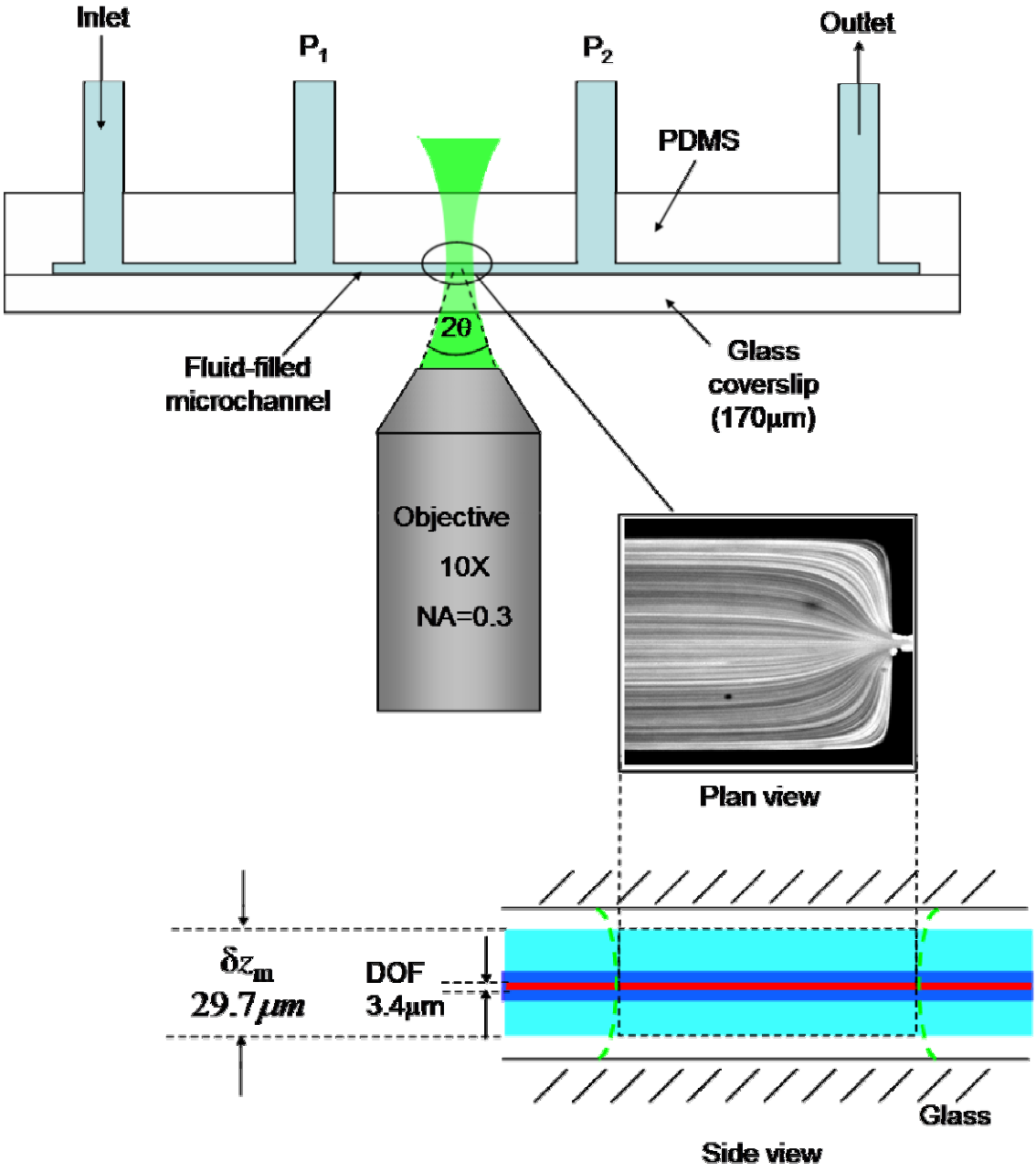

Figure 6. Flow visualisation set-up; fluorescence imaging of 1.1 micron particles using a 10X 0.3NA objective and long exposure to generate streak images. The measured pressure drop is given by, $\Delta P_{12}=P_1-P_2$.

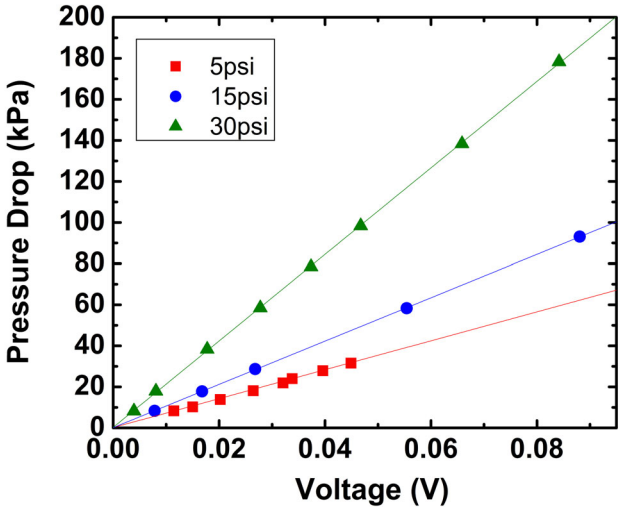

Figure 7 (a). Calibration data for three differential pressure sensors, able to measure maximum differential pressures of ΔP_{12} = 34.5kPa, 103kPa, and 207kPa. These are denoted by 5psi, 15psi, and 30psi, respectively.

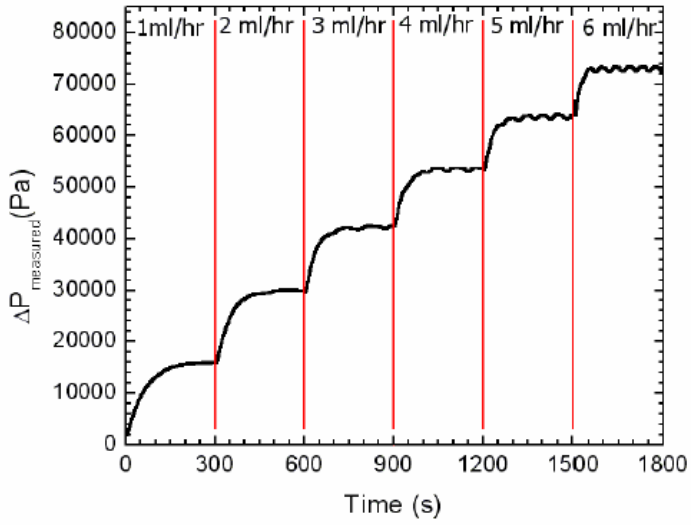

Figure 7(b). Transient pressure response of the system for increasing flow rates (0 ml/hr - 6 ml/hr). Flowrates from the syringe pump are increased 1 ml/hr every 5 minutes. Measurements are performed using a Newtonian 55% glycerol and water mixture (η_0 = 8.59 mPa.s) in a 400:25 μm contraction. The system response time is on the order of 5 minutes at the lowest flow rates, but decreases as the flow rate increases.

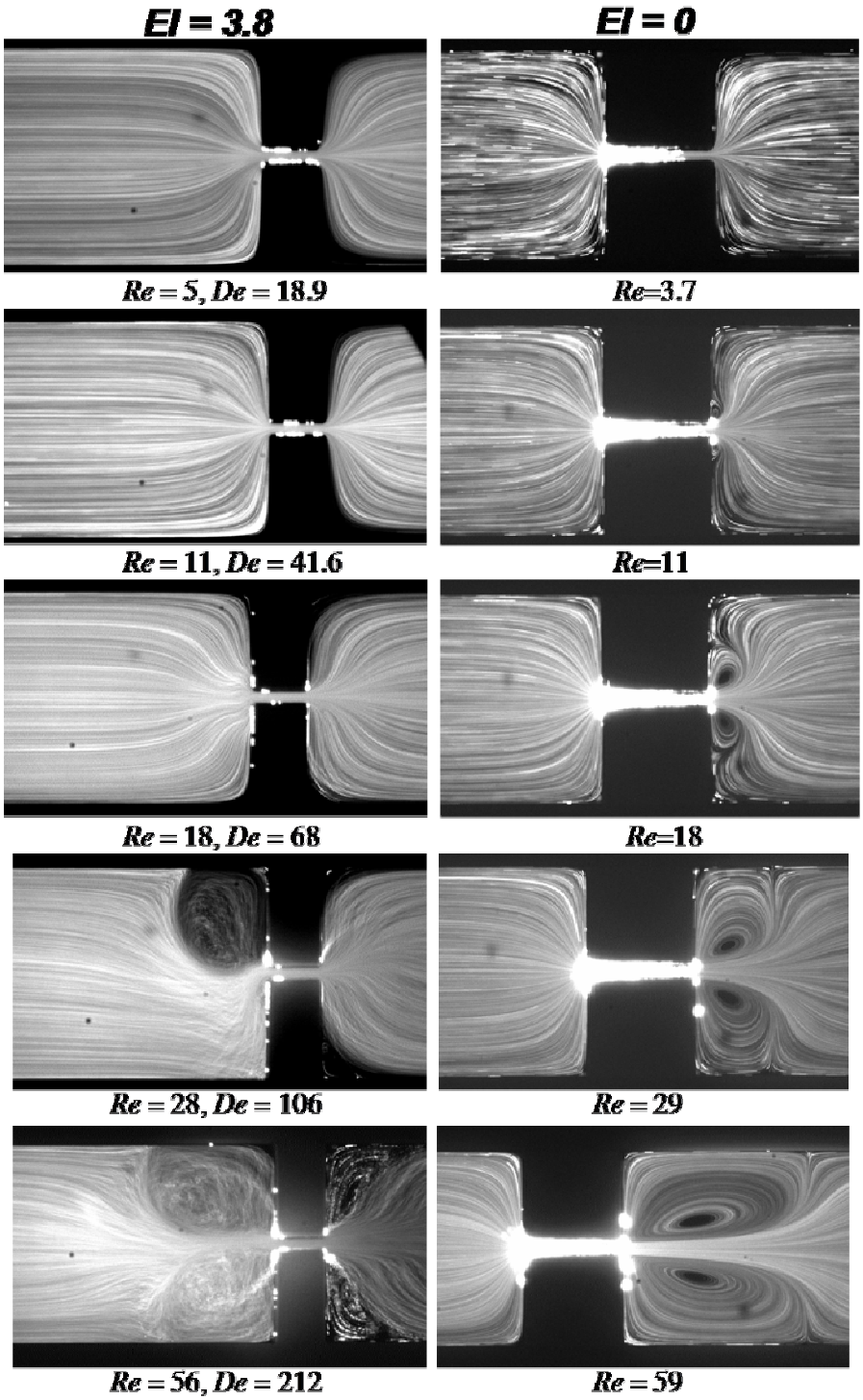

Figure 8. Comparison of Newtonian and non-Newtonian entrance planar entry flows at the same *Re*; (a) 0.05% PEO (*El* = 3.8) and (b) DI water (*El* = 0) in a 16:1 contraction-expansion for 4 d *Re* d 60. The length of the contraction of the geometry containing the Newtonian fluild, L_c = 200 is twice that of the geometry containing the elastic fluid, L_c = 100. Flow is from left to right.

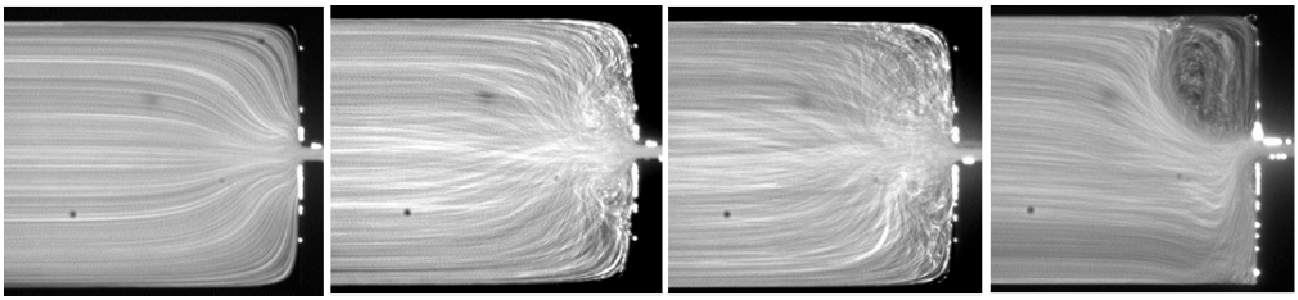

Figure 9. The development of streaklines in the flow of 0.05% PEO (*El* = 3.8) in the 16:1 planar contraction during the transition from bending streamlines to vortex growth regimes. For this fluid, this transition occurs over the range of flowrates ($4.5 \leq Q \leq 6$ ml/hr) corresponding to $18 \leq Re \leq 24$ and $68 \leq De \leq 91$.

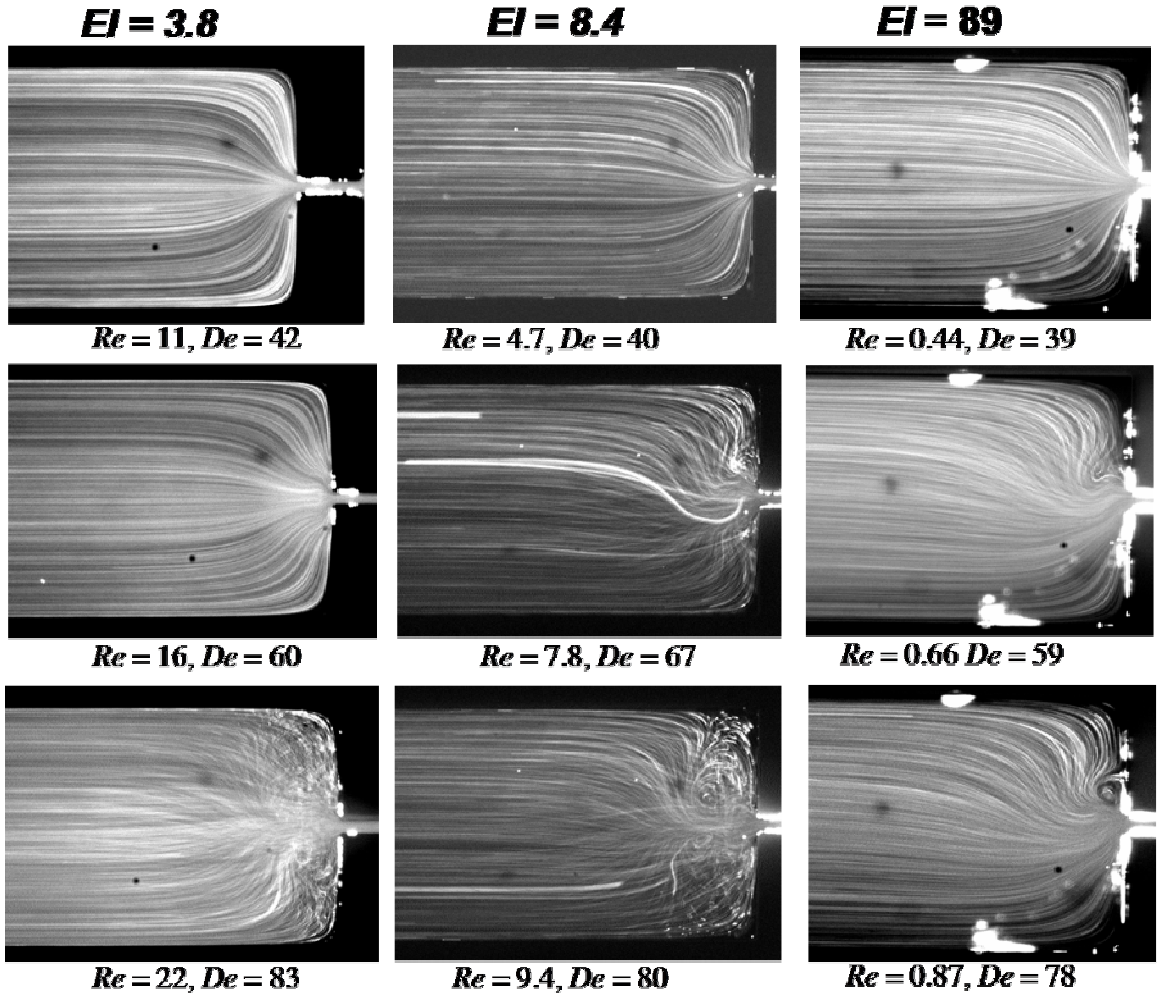

Figure 10. Effect of the elasticity number on upstream flow patterns; streak images of 0.05% PEO (*El* = 3.8), 0.1% PEO (*El* = 8.4) and 0.3% PEO (*El* = 89) flowing through a 16:1 planar contraction around the onset of non-Newtonian behaviour, compared at the same value of the Deborah number, 40 d *De* d 80.

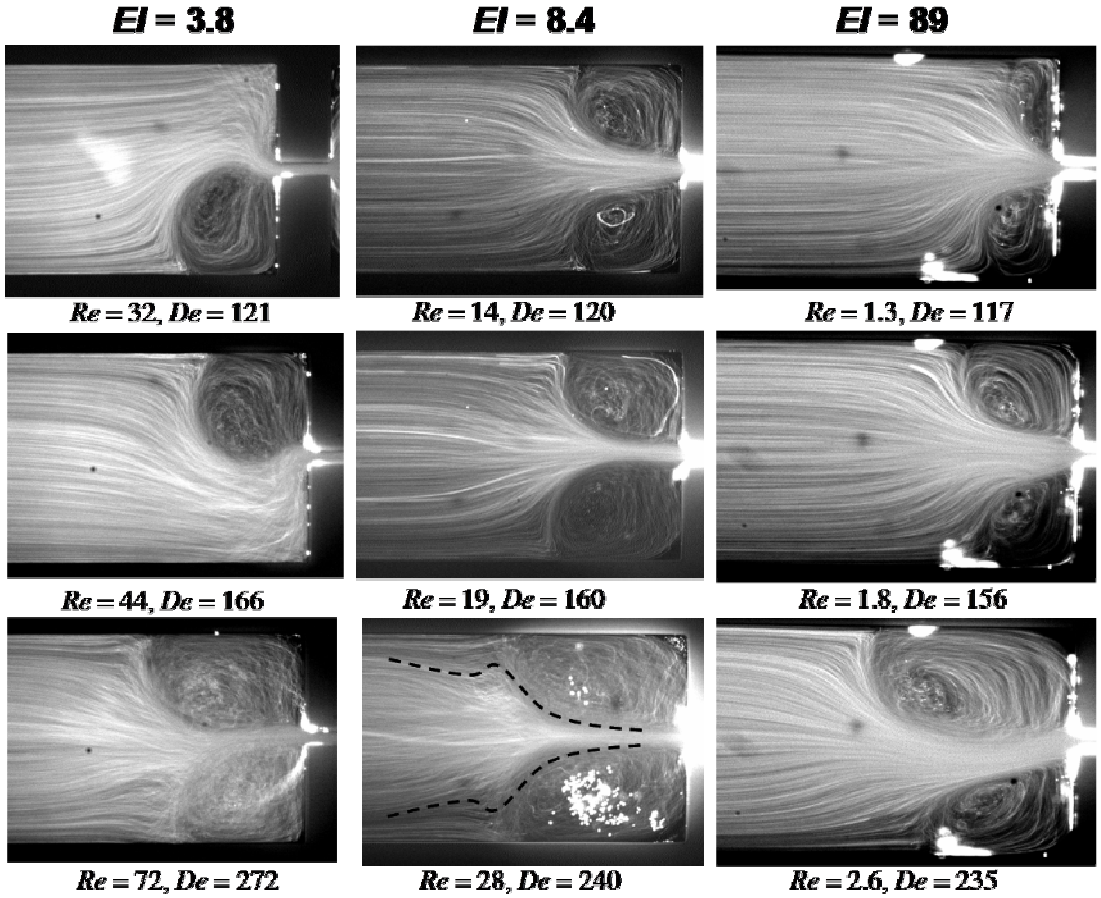

Figure 11. Effect of the elasticity number on upstream flow patterns; streak images of 0.05% PEO (*El* = 3.8), 0.1% PEO (*El* = 8.4) and 0.3% PEO (*El* = 89) flowing through a 16:1 planar contraction during the vortex growth regime compared at the same values of the Deborah number, 215 d *De* d 280.

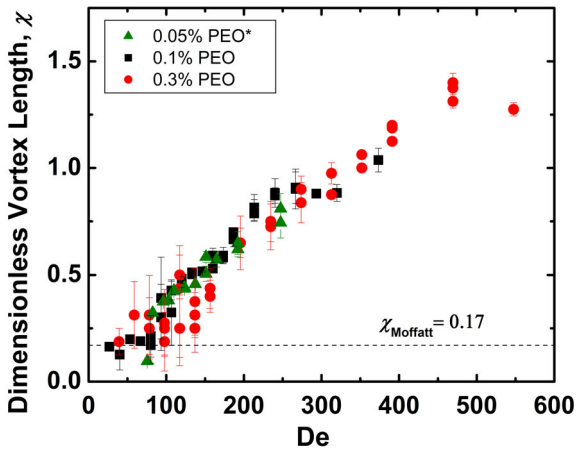

Figure 12. Dimensionless vortex length as a function of *De*; (▲) 0.05% PEO (*El* = 3.8), (■) 0.1% PEO (*El* = 8.4) and (•) 0.3% PEO (*El* = 89).

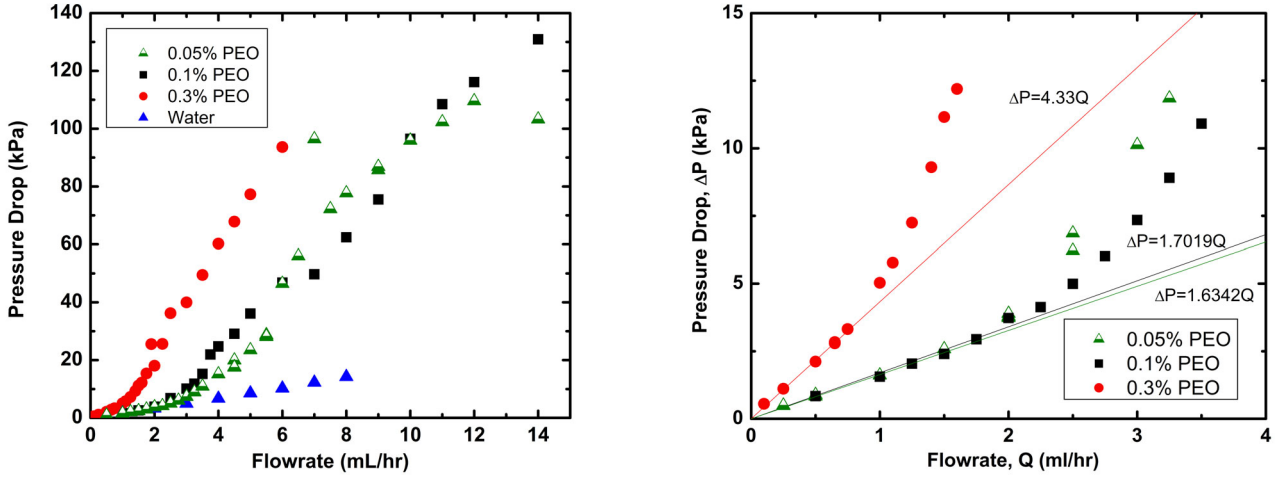

(a) (b)

Figure 13. Total Pressure drop (ΔP_{12}) versus flowrate (Q) for the (Δ) 0.05% PEO, (■) 0.1% PEO, (•) 0.3% PEO polymer solutions and for (▲) water flowing through a 16:1 planar contraction; (a) all data and (b) determining slope at low flowrates for normalizing pressure data

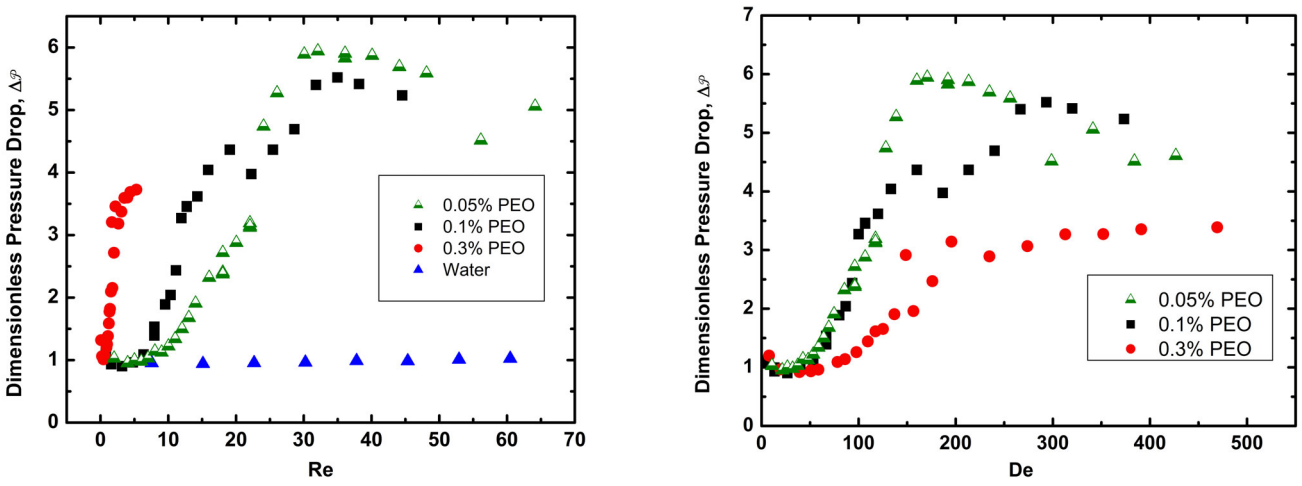

(a) (b)

Figure 14. Dimensionless pressure drop versus (a) *Re* and (b) *De* for (Δ) 0.05% PEO, (■) 0.1% PEO, (●) 0.3% PEO and (▲) water ((a) only) in a 16 :1 planar contraction

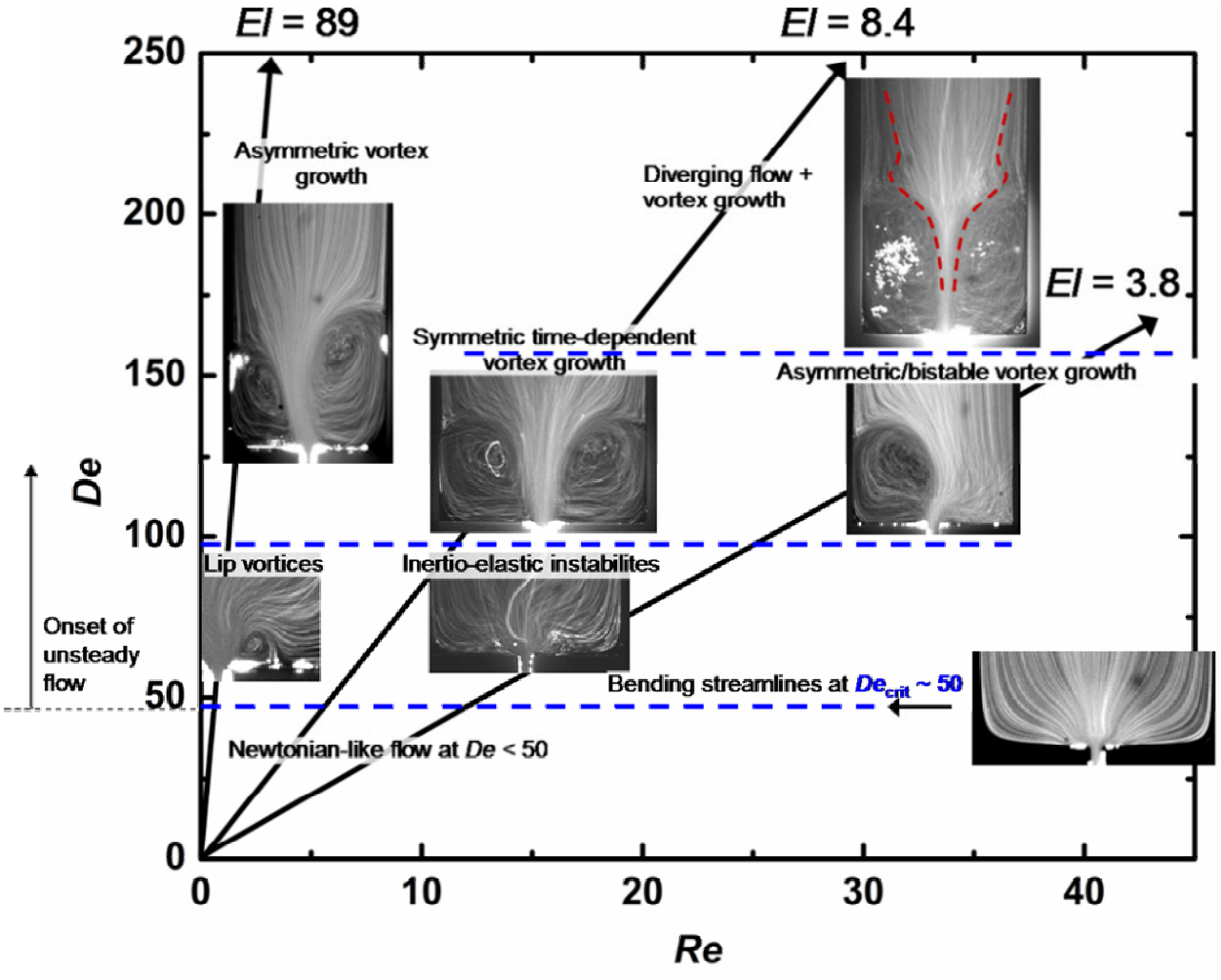

Figure 15. Summary of flow regimes in *De*-*Re* space for semi-dilute aqueous PEO solutions through micro-fabricated geometries